Crystallographic preferred orientation (CPO) development governs the strain weakening in minerals with strong viscous anisotropy at high homologous temperatures ([?] 0.9): insights from up-strain ice deformation experiments

Sheng Fan[1], Andrew J. Cross[2], David J. Prior[1], David L. Goldsby[3], Travis F. Hager[3], Marianne Negrini[1], and Chao Qi[4]

[1]University of Otago
[2]Woods Hole Oceanographic Institution
[3]University of Pennsylvania
[4]Institute of Geology and Geophysics, Chinese Academy of Sciences

November 23, 2022

Abstract

Strain weakening plays an important role in the continent-scale flow of rocks and minerals, including ice. In laboratory experiments, strain weakening coincides with microstructural changes including grain size reduction and the development of crystallographic preferred orientation (CPO). To interrogate the relative contributions of CPO development and grain size towards the strain weakening of viscously anisotropic minerals at very high homologous temperatures (Th [?] 0.9), we deformed initially isotropic polycrystalline ice samples to progressively higher strains. We subsequently combined microstructural measurements from these samples with ice flow laws to separately model the mechanical response arising from CPO development and grain size reduction. We then compare the magnitudes of strain weakening measured in laboratory experiments with the magnitudes of strain weakening predicted by the constitutive flow laws. Strain weakening manifests as strain rate enhancement after minimum strain rate under constant load conditions, and as a stress drop after peak stress under constant displacement rate conditions. However, flow laws that only consider grain size evolution predict a nominally constant sample strength with increasing strain. On the other hand, flow law modelling that solely considers CPO effects can accurately reproduce the experimental strain weakening measurements. These observations suggest that at high homologous temperatures (Th [?] 0.9), CPO development governs the strain weakening behaviour of viscously anisotropic materials like ice. Grain size, on the other hand, plays a negligible role in strain weakening under such conditions. Overall, we suggest that geodynamic and glaciological models should incorporate evolving CPOs to account for strain weakening, especially at high homologous temperatures.

Crystallographic preferred orientation (CPO) development governs the strain weakening in minerals with strong viscous anisotropy at high homologous temperatures (≥ 0.9): insights from up-strain ice deformation experiments

Sheng Fan[1], Andrew J. Cross[2,3], David J. Prior[1], David L. Goldsby[3], Travis F. Hager[3], Marianne Negrini[1], Chao Qi[4]

[1] Department of Geology, University of Otago, Dunedin, New Zealand

[2] Department of Geology and Geophysics, Woods Hole Oceanographic Institution, Woods Hole, MA, USA

[3] Department of Earth and Environmental Science, University of Pennsylvania, Philadelphia, PA, USA

[4] Institute of Geology and Geophysics, Chinese Academy of Sciences, Beijing, China

Corresponding author: Sheng Fan (sheng.fan@otago.ac.nz)

Key Points:

- We use ice deformation experiments to quantify the contributions of grain size reduction and CPO development to strain weakening at $T_h \geq 0.9$.
- Ice flow laws are used to model the mechanical response to changes in CPO and grain size; the results are compared with mechanical data.
- At high temperatures ($T_h \geq 0.9$), CPO development governs strain weakening, whereas grain size evolution plays a negligible role.

Abstract

Strain weakening plays an important role in the continent-scale flow of rocks and minerals, including ice. In laboratory experiments, strain weakening coincides with microstructural changes including grain size reduction and the development of crystallographic preferred orientation (CPO). To interrogate the relative contributions of CPO development and grain size towards the strain weakening of viscously anisotropic minerals at very high homologous temperatures (T_h≥0.9), we deformed initially isotropic polycrystalline ice samples to progressively higher strains. We subsequently combined microstructural measurements from these samples with ice flow laws to separately model the mechanical response arising from CPO development and grain size reduction. We then compare the magnitudes of strain weakening measured in laboratory experiments with the magnitudes of strain weakening predicted by the constitutive flow laws. Strain weakening manifests as strain rate enhancement after minimum strain rate under constant load conditions, and as a stress drop after peak stress under constant displacement rate conditions. However, flow laws that only consider grain size evolution predict a nominally constant sample strength with increasing strain. On the other hand, flow law modelling that solely considers CPO effects can accurately reproduce the experimental strain weakening measurements. These observations suggest that at high homologous temperatures (T_h≥0.9), CPO development governs the strain weakening behaviour of viscously anisotropic materials like ice. Grain size, on the other hand, plays a negligible role in strain weakening under such conditions. Overall, we suggest that geodynamic and glaciological models should incorporate evolving CPOs to account for strain weakening, especially at high homologous temperatures.

Plain Language Summary

The strength of ice and other miners becomes weakened during the deformation, and such material characteristic plays a key role in shaping the earth, such as the formation of shear zones. In this study, we deform ice samples to progressively higher strains. The microstructural data of ice samples are used to predict the strength of ice. The results show, at temperatures close to the ice melting point, grain size change has little control on the reduction of ice strength. On the other hand, the progressive alignment in the orientations of ice crystals dominates the ice strength reduction during the deformation.

1 Introduction

Strain weakening enables high-temperature creep deformation to localize into narrow lithospheric shear zones (e.g., Bestmann & Prior, 2003; Little et al., 2015; Skemer et al., 2009; White et al., 1980) and cryospheric shear margins (e.g., Gerbi et al., 2021; Gow & Williamson, 1976; Jansen et al., 2016), and therefore plays a central role in plate tectonics and ice discharge, respectively. In order to accurately model these large-scale processes, we need a comprehensive understanding of the microphysical processes that produce strain weakening across a broad range of conditions. Many studies have linked mechanisms such as grain size evolution, CPO development, melt band formation, metamorphic reactions and transformations, water weakening and mineral phase mixing and/or layering to strain weakening at relatively low homologous temperatures (T_h<0.7) (e.g., Poirier, 1980; S. H. White et al., 1980). However, we have a somewhat limited understanding of the processes that produce strain weakening in rocks and minerals at very high temperatures (T_h>0.7) and, crucially, their influence over mechanical strength and strain weakening. This is because rock deformation experiments at T_h much higher than 0.7 are difficult—most rock deformation rigs are limited to temperatures <1500 K, whereas many major rock-forming minerals have much higher melting temperatures (e.g., ~1950 K for quartz, ~2200 K for olivine). On the other hand, it is much easier for ice to reach T_h≥0.9 under experimental conditions. Therefore, ice provides an analogue to understand the strain weakening mechanism during the high-temperature deformation of other viscously anisotropic minerals, such as quartz and olivine (Wilson et al., 2014).

Ice creep experiments show that the strength of initially-isotropic polycrystalline ice evolves during deformation (Glen, 1955; Jacka & Maccagnan, 1984; Mellor & Cole, 1982). Strain weakening occurs after secondary creep (i.e., minimum strain rate) in constant load experiments (Budd & Jacka, 1989; Weertman, 1983) and after peak stress in constant displacement rate experiments (Durham et al., 1983; Fan et al., 2020; Qi et al., 2017; Vaughan et al., 2017). At the bulk sample scale, enhancement invariably coincides with grain size evolution and/or the development of a crystallographic preferred orientation (CPO) (Fan et al., 2020).

CPOs arise from the collective glide of dislocations (and accompanying rotation of crystal lattice planes) during deformation. Since dislocation glide on the ice basal plane (0001) is at least sixty times easier than glide on any other crystallographic plane (Duval et al., 1983), ice exhibits a strong viscous anisotropy. As a result, ice grains typically rotate via—and in order to maximize—shearing on the basal plane during deformation (Castelnau et al., 1996; Llorens et al., 2016; van der Veen & Whillans, 1994). Thus, CPOs in ice are typically defined by an alignment of *c*-axes (poles to basal planes). Furthermore, deformation experiments on ice polycrystals containing a strong, pre-existing CPO show that samples with basal planes better aligned to accommodate slip can deform more easily (e.g., Gao and Jacka, 1987; Lile, 1978; Shoji and Langway, 1988, 1984). For example, under uniaxial compression, polycrystalline ice samples with basal planes inclined 45° from the compression axis are at least five times weaker than polycrystalline ice samples with basal planes sub-parallel or sub-perpendicular to the compression axis (Shoji & Langway, 1988). Similarly, during simple shear, ice samples with basal planes aligned with the shear plane are at least one order of magnitude weaker than ice samples with basal planes highly oblique to the shear plane (Lile, 1978; Shoji & Langway, 1984). Given these observations, and the extreme viscous anisotropy of ice, many studies of ice sheet mechanics assume that strain rate enhancement (i.e., strain weakening) is caused solely by CPO development (e.g., Azuma, 1995, 1994; Hruby et al., 2020; Morland and Staroszczyk, 2009; Placidi et al., 2010). Recently, modelling works from Rathmann & Lilien (2021) show enhancement (which they attribute solely to CPO) must be accounted for in order to accurately infer basal friction of ice mass. Accordingly, constitutive ice flow laws are often modified using *ad hoc* scalar "enhancement factors", which account for CPO development under specific thermomechanical conditions, loading geometries, and for ice samples with different ages and impurity contents (see review by Cuffey & Paterson, 2010, pp. 77). Moreover, some works have also sought to quantify the relationship between enhancement and CPO development as a continuous function of strain and loading geometry (e.g., Azuma, 1995, 1994; Budd et al., 2013; Morland and Staroszczyk, 2009; Placidi et al., 2010). Nevertheless, such models likewise assume that CPO development is the dominant source of strain weakening.

In the study of metals and minerals other than polycrystalline ice, researchers also invoke grain size reduction as a source of strain weakening (Drury, 2005; McQueen & Jonas, 1975; Rutter, 1999; Sellars, 1978). Grain size reduction arises from the combined operation of dynamic recovery and recrystallization, which remove ("annihilate") and reorganize linear defects (dislocations) into low-energy configurations, thereby relaxing the internal stress state of grains and counteracting work hardening caused by dislocation multiplication and interaction (Derby & Ashby, 1987; Duval, 1979; Humphreys et al., 2017; Weertman, 1983). Grain size reduction also enhances grain size sensitive (GSS) creep mechanisms (Bestmann & Prior, 2003; A. J. Cross & Skemer, 2017; Warren & Hirth, 2006) including volume self-diffusion, grain boundary diffusion, and grain boundary sliding, which dominate at fine grain sizes (Frost & Ashby, 1982; Raj & Ashby, 1971). In the GSS creep regime, crystalline materials weaken as grain size decreases (Frost & Ashby, 1982). Thus, grain size reduction is widely proposed as a source of strain localization within Earth's lithosphere (Braun et al., 1999; De Bresser et al., 2001; Drury, 2005; Etheridge & Wilkie, 1979; Kilian et al., 2011; Rutter & Brodie, 1988) and may conceivably also contribute to strain weakening in ice.

Although it is well established that strain weakening coincides with both grain size reduction and CPO development, the relative contributions of these two processes towards enhancement in ice, and in other minerals at high homologous temperatures (T_h>0.7), remains unclear. This uncertainty largely arises because CPO development and grain size evolution are strongly coupled and coevolve during deformation (Fan et al., 2020; Piazolo et al., 2013). As such, it is difficult to deconvolve their individual and relative effects. Many experiments have been performed to large strains (>10%) to determine the steady-state mechanical properties of water ice (e.g., Durham et al., 1983; Qi et al., 2017). However, while these experiments exhibit strain weakening behaviour, understanding which mechanisms govern weakening is not easy from the examination of steady-state microstructures alone. Experiments to successively higher strains—through the transition from secondary creep (or peak stress) to tertiary creep (or flow stress) (Fan et al., 2020, 2021a; Jacka & Maccagnan, 1984; Piazolo et al., 2013)—provide more information about the microphysical processes that control strain weakening. Yet, to date, the majority of laboratory deformation experiments have been performed under uniaxial compression conditions and at temperatures ≥ -10°C (Jacka & Maccagnan, 1984; Piazolo et al., 2013; Vaughan et al., 2017). Under such conditions, ice develops a CPO characterized by a *c*-axis small circle (open cone) around the compression axis, indicating that the microstructure evolves to maximize easy (basal) slip conducive to strain weakening. Polar ice sheets and extra-terrestrial cryospheres, on the other hand, can experience ambient temperatures much colder than -10 °C (Journaux et al., 2020; Kamb, 2001). Recent experiments performed at temperatures between -30 and -10 °C show that ice *c*-axes instead evolve from an open cone towards a single cluster parallel to compression as temperature decreases (Fan et al., 2020; Fan et al., 2021a) or as stress increases (Qi et al., 2017). The transition from cone-shaped to cluster-shaped *c*-axes CPO indicate many ice-basal-planes rotate from easy (basal) to hard (compression-normal) slip orientations. Therefore, it is necessary to evaluate the impact of CPO development on strain weakening.

At low stresses (typically <0.1 MPa), water ice exhibits GSS creep behaviour that arises from coupled grain boundary sliding (GBS) plus basal dislocation glide (easy slip), and diffusion (Durham et al., 2010; Goldsby & Kohlstedt, 2001; Goldsby & Kohlstedt, 1997). At relatively high stresses (>1 MPa), grain size reduction, which results from the production of new small grains at the cost of original big grains, can be observed with an increasing strain; the CPO of small-grain population is weakened at a lower temperature (<-10 °C), indicating a randomization of small-grain orientations (Fan et al., 2020). The CPO weakening of small-grain population is considered as a signal for GBS within deformed rock (Bestmann & Prior, 2003; Warren & Hirth, 2006). Therefore, GBS is proposed as a candidate mechanism for CPO weakening within small ice grains at low temperatures (T<-10 °C). Grain size evolution may therefore also affect strain weakening in ice polycrystals if grain size reduction is sufficiently enough to activate a significant component of GSS creep. Indeed, a composite flow law incorporating terms for these various GSI and GSS mechanisms (Goldsby & Kohlstedt, 2001) has recently been used to model terrestrial ice deformation (Behn et al., 2020; Kuiper, et al., 2020a, 2020b). The modelling results show predicted strain rate in fine-grained ice layers (deposited during the last Glacial maximum) is much faster than the coarse-grained Holocene ice (Kuiper et al., 2020a). Moreover, variations in polar ice flow, which cannot be explained by Glen's flow law, might be explained by strain rate enhancement caused by localized grain size variations (Behn et al., 2020).

This study aims to quantify the relative contributions of grain size reduction and CPO development towards the strain weakening (enhancement) of ice at temperatures between -30 °C and -4 °C (T_h = 0.89–0.99). First, we present the mechanical responses of samples deformed to successively higher strains through the transition from secondary creep to tertiary creep in constant load experiments at -4 °C, or through the transition from peak stress to flow stress in constant displacement rate experiments at -10 and -30 °C. Second, we quantify the microstructure of each deformed sample using cryogenic electron backscatter diffraction (cryo-EBSD; Prior et al., 2015), focussing largely on grain size and CPO evolution. Finally, we combine our microstructural measurements with ice flow laws (Azuma, 1995; Durham et al., 1983; Glen, 1955; Goldsby & Kohlstedt, 2001) to try and reproduce the mechanical responses of the experimental samples as a function of strain, using grain size and CPO measurements as model inputs. We compare those modelled stresses and strain rates to the measured (actual) mechanical data to estimate how much of the mechanical response is due to the evolution of grain size and/or CPO under different experimental conditions.

2 Methods

2.1 Experimental data

2.1.1 Sample fabrication

Ice samples with controlled initial grain size, random CPO and minimised porosity were fabricated using a flood-freeze method (Cole, 1979). Ice cubes made from ultra-pure deionized water were crushed and sieved at -30 °C to produce ice powders with particle sizes between 180 and 250 μm. These ice powders were packed into greased cylindrical moulds to achieve a porosity of ~40%. Degassed ultra-pure deionized water (0 °C) was flooded into the packed moulds, which had been evacuated to a near-vacuum state and equilibrated at 0 °C in a water-ice bath for ~40 minutes. The flooded moulds were immediately transferred to a -30 °C chest freezer and placed vertically on a copper plate for ~24 hours. During this step, we used polystyrene to insulate the cylinders from all the other sides to ensure the freezing front migrates upwards slowly from the bottom, minimizing the entrapment of bubbles within the samples.

Ice samples, which after freezing had a mean grain size of ~300 μm (Fan et al., 2020), were gently pushed out from the moulds using an Arbor press. These fine-grained ice samples were fabricated with a cylinder diameter of 25.4 mm. We accidently also produced medium-grained ice samples, with a mean grain size of ~550 μm (Fan et al., 2021a), by leaving the frozen, flooded samples in the water-ice bath for ~30 minutes before extraction. The medium-grained ice samples were fabricated with a cylindrical diameter of 27 mm. All samples were cut such that their length was 1.5–2 times of their diameter. After cutting, samples were polished on both ends to ensure they were flat and perpendicular to the cylinder axis. After polishing, the initial sample length, L_0, was measured using a caliper.

2.1.2 Deformation assembly

Medium-grained ice samples were used for constant load experiments, performed using a 1-atm (unconfined), dead-weight creep apparatus in the Ice Physics Laboratory, University of Otago (Fan et al., 2021a). Each ice sample was encapsulated in a rubber jacket together with a walnut wooden platen and a walnut wooden piston (Fan et al., 2021a). Encapsulation of the deformation assembly was processed in a -30 °C chest freezer. These experiments were conducted at a temperature of -4 ± 0.2 °C under a constant load of 60 kg, yielding an initial stress of ∼1.0 MPa (Fan et al., 2021a). Experiments were terminated once the true axial strain, ε, reached ~1, 4, 8, 13%. We did not apply a stiffness correction to account for elastic deformation of the walnut piston and platen; however, the elastic strain expected in walnut at 1 MPa differential stress is negligible (Appendix A).

Fine-grained ice samples were used for constant displacement rate experiments, performed in a cryogenic triaxial apparatus (Heard et al., 1990), with a nitrogen gas confining pressure of 20–40 MPa at -10 ± 0.5°C and -30 ± 0.5°C, in the Ice Physics Laboratory, University of Pennsylvania. Each ice sample was encapsulated in a thin-walled indium jacket tube (~0.38 mm wall thickness) with the bottom already welded to a stainless-steel end-cap. The top of indium jacket tube was then welded to a steel semi-internal force gauge, with a thermally insulating zirconia spacer placed between the force gauge and sample. The sample was kept cold in a -60 °C ethanol bath during welding. Most of the experiments were conducted under constant displacement rates yielding initial strain rates, $\dot{\varepsilon}$, of ~$1 \times 10^{-5} s^{-1}$; these experiments were terminated once the strain, ε, reached ~3%, 5%, 8%, 12% and 20%. The rest of these experiments were conducted at -30 ± 0.5 °C with $\dot{\varepsilon}$ of ~$5 \times 10^{-5} s^{-1}$; these experiments were terminated once ε reached ~3% and ~20%.

2.1.3 Experimental procedures and data processing

All experiments presented in this study were conducted under uniaxial compression loading conditions (Fig. 1(a)). Before the start of each experiment, samples were left to thermally equilibrate with the deformation apparatus for at least 60 minutes at experiment (pressure, temperature) conditions before deformation commenced. After each experimental run, ice samples were immediately extracted from the apparatus, photographed, and measured. To minimize thermal cracking, samples were progressively cooled to ~ -30, -100 and -196 °C over a period of ~15 minutes, and thereafter stored in a liquid nitrogen dewar. We note that during the time frame of sample extraction, transportation, and preparation for cryo-EBSD, normal grain growth should be negligible (Fan et al., 2021b) and significant modifications in grain CPO are unlikely (Wilson et al., 2014)

The processed mechanical data are shown in Tables 1(a), 1(b). During each experimental run, time, t, and vertical shortening of the ice sample, $s(t)$, were recorded every 3–5 seconds. The true axial strain, $\varepsilon(t)$, is calculated from the initial ice sample length, L_0, and vertical sample shortening, $\Delta L(t)$ (Eq. (1)).

$$\varepsilon(t) = -\ln\left(\frac{L_0 - \Delta L(t)}{L_0}\right) \tag{1}$$

The true axial strain rate, $\dot{\varepsilon}(t)$, is calculated from the true axial strain interval during time interval, Δt (Eq. (2)).

$$\dot{\varepsilon}(t) = \frac{\varepsilon(t) - \varepsilon(t - \Delta t)}{\Delta t} \tag{2}$$

Differential stress, σ, was calculated from the axial load, $F(t)$, and cross-sectional area of the ice sample. For constant load experiments, $F(t) = 60\ kg \times 9.81\ N/kg = 588.6\ N$. For constant displacement rate experiments, $F(t)$, was recorded every 3-5 seconds. Differential stresses have been corrected for the change of sample cross-sectional area during deformation, assuming constant sample volume:

$$\sigma(t) = \frac{F(t)}{\pi R(t)^2}, \tag{3}$$

where $R(t) = R_0\sqrt{\frac{L_0}{L_0 - \Delta L(t)}}$ is the sample radius at time t.

In this study, unless specified, the term "strain" represents the bulk true axial strain; the term "strain rate" represents the axial true axial strain rate; the term "stress" represents the differential stress.

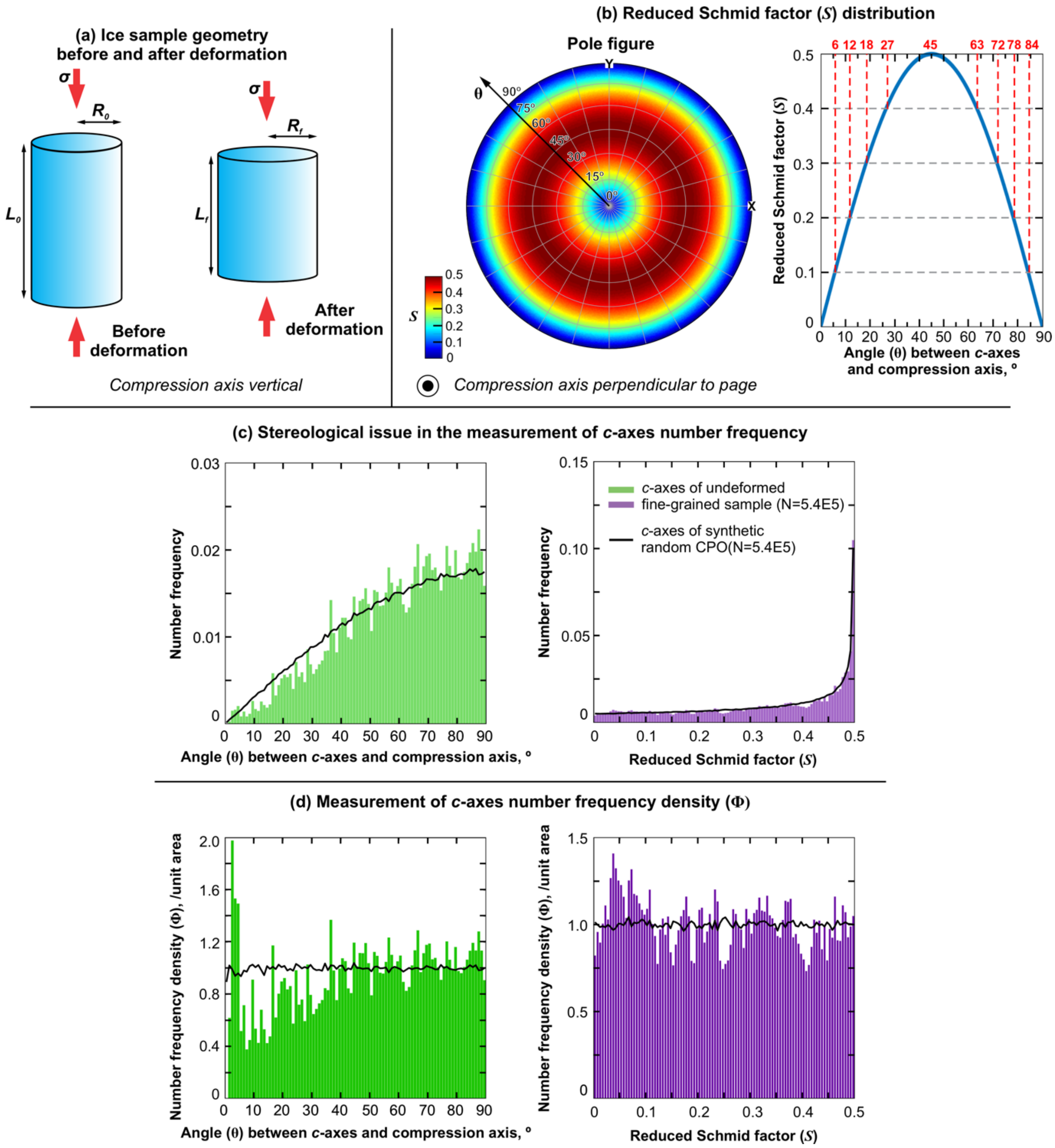

Figure 1. (a) Schematics of the ice samples before and after deformation for uniaxial compression. **(b)** Distribution of modelled reduced Schmid factor, ***S*** (Sect. 2.4.2). The left panel shows a pole figure with 1E6 randomly generated *c*-axes points, with the compression axis normal to page. Each *c*-axis point is coloured by its corresponding ***S***, which is a function of the angle between *c*-axis and compression axis, ***θ*** (Eq. (11)). The right panel shows the value of ***S*** for *c*-axes with different angles to compression (***θ***). **(c)** Illustrating the stereological issue in the measurement of *c*-axes number frequency using the undeformed fine-grained ice as an example. Bar plots show the number frequency of measurements at each interval of the angle between *c*-axes and compression (***θ***) (coloured green) or at each interval of reduced Schmid factor, *S* (coloured purple). **(d)** The number frequency density, **Φ** (Sect. 2.4.2; Appendix D), statistics using the undeformed fine-grained ice as an example. Bar plots show **Φ** of measurements at each interval of the angle between c-axes and compression (***θ***) (coloured green) or at each interval of reduced Schmid factor, *S* (coloured purple). The Black curves represent the distribution of number frequency (**(c)**) or number frequency density, **Φ** (**(d)**), for artificially generated CPO with the same number of points as the undeformed fine-grained ice.

Table 1(a). Summary of the mechanical and grain size data for uniaxial compression experiments with constant load

Large table presented at the end of this manuscript as well as in a separate spreadsheet.

Table 1(b). Summary of the mechanical and grain size data for uniaxial compression experiments with constant displacement rate

Large table presented at the end of this manuscript as well as in a separate spreadsheet.

2.2. Microstructural data

2.2.1 EBSD data collection

To quantify grain size distributions and CPOs, we analysed each sample using cryogenic electron backscatter diffraction (cryo-EBSD). We prepared the ice samples and acquired cryo-EBSD data following the procedures described by Prior and others (2015). A Zeiss Sigma VP FEG-SEM combined with either an Oxford Instruments NordlysF or Symmetry EBSD camera was used for the data collection (the EBSD camera was upgraded partway through this study). Raw EBSD data were montaged using Oxford Instruments' AZtec software. For fine-grained ice samples, we collected reconnaissance maps with a step size of 30 μm from the whole section and, for detailed microstructural analyses, maps with a 5 μm step size from selected sub-areas. For medium-grained ice samples, we collected EBSD data with a step size of 30 μm from the whole section.

2.2.2 EBSD data processing

Ice grains were reconstructed from raw EBSD pixel maps using a Voronoi decomposition algorithm in the MTEX toolbox (Bachmann et al., 2011). Grains were defined using a grain boundary misorientation angle threshold of 10°. No pixel interpolation was applied to the raw EBSD data, which generally indexed at a rate close to or higher than 90%. After grain reconstruction, we removed grains with area equivalent diameter larger than 20 μm (for maps with 5 μm step size) or 120 μm (for maps with 30 μm step size), which are likely to result from mis-indexing. We also removed grains truncated by the edges of maps, and removed poorly constrained grains (i.e., grains with <50% indexed pixel coverage). To clearly reveal the CPO patterns, contoured pole figures were constructed from the filtered EBSD maps with 30 μm step size, using all pixels indexed as ice-1h, and a contouring half-width of 7.5°. Grain size was calculated from the filtered EBSD maps with 5 μm and 30 μm step size for the fine-grained and medium-grained samples, respectively.

2.3 Mechanical models

In this study, we attempt to model (i.e., reproduce) the transient evolution of ice strength—i.e., the experimental stress-strain and strain rate-strain curves—using ice flow laws that account, separately, for changes in grain size (Goldsby & Kohlstedt, 1997, 2001) and CPO (Azuma, 1994, 1995). We constrain the models using grain sizes and CPOs measured from each experimental sample, representing the microstructural state at fixed strain intervals. Strictly speaking, the flow laws used in this study describe the rheological behaviour of ice only under steady state (strain invariant) conditions; that is, under conditions where strain rate and stress do not change significantly with increasing strain. Our modelling approach is therefore based on a key assumption that at each infinitesimal strain increment, the ice aggregate deforms at a quasi-steady-state (e.g., Holtzman et al., 2018). Recent studies (e.g., Soleymani et al., 2020) have found that the microstructural state lags behind the mechanical state; in other words, it takes some time for the microstructure to respond to changes in stress and/or strain rate. However, this lag is generally insignificant at very high homologous temperatures (Soleymani et al., 2020), as is the case here, due to rapid recovery and recrystallization at high temperatures (Cross & Skemer, 2019; Fan et al., 2020; Fan et al., 2021a; Holtzman et al., 2018).

2.3.1 Mechanical response without microstructural evolution

As a reference, we calculate the strength predicted by the microstructure-insensitive constitutive flow laws of Glen (1955) and Durham et al. (1983). These flow laws were derived from laboratory experiments on relatively coarse grained samples, where creep is assumed to proceed solely via grain size insensitive (GSI) dislocation glide and climb (i.e., dislocation creep). Strain contributions from grain size sensitive (GSS) mechanisms (outlined in Sect. 2.3.2) were assumed to be negligible in the experiments used to derive the GSI flow laws. These flow laws also do not explicitly account for enhancement due to CPO development. Glen's flow law describes secondary creep, derived using bulk strain rate minimum data for ice deformed under constant load/stress (Glen, 1955). In secondary creep, polycrystalline samples remain nominally untextured (i.e., random CPO). Durham's flow law, on the other hand, was derived from flow stresses measured at high strains (usually >10% sample shortening) for ice samples deformed in uniaxial compression under constant displacement rates (Durham et al., 1983). Thus, Durham's flow law may implicitly incorporate the mechanical effects of CPO development and grain size, as ice deformed to >10% strain typically undergoes appreciable recrystallization and CPO development (Fan et al., 2020).

Glen's and Durham's flow laws can be expressed in the general form:

$$\dot{\varepsilon} = A\sigma^n \exp\left(-\frac{Q}{RT}\right), \quad (4)$$

where A ($MPa^{-n}m^p s^{-1}$) is a material-dependent parameter, σ (MPa) is the bulk stress, n is the stress exponent, R ($= 8.314 \times 10^{-3}$ $kJmol^{-1}K^{-1}$) is the gas constant, and T (K) is the absolute temperature. Q ($kJmol^{-1}$) is the activation energy for Glen's flow law, and it is the activation enthalpy for Durham's flow law. Parameters for Glen's flow law were taken from Kuiper et al. (2020a, 2020b); parameters of Durham's flow law were taken from Durham et al. (1983), and they are summarised in Table 2. Glen's experiments yielded n (stress exponent) values of between 3.2 and 3.3 for secondary creep, though Glen suggested that n rises to values around 4 at higher strains (Glen, 1952, 1953, 1955). Paterson (1994) later defined "Glen's flow law" with n = 3, and this form is now used almost ubiquitously across the ice modelling literature (Gillet-Chaulet et al., 2012; Graversen et al., 2011; Hruby et al., 2020). Durham's flow law, on the other hand, has $n = 4$ and matches other measurements of the stress exponent at steady state under relatively large stresses (Goldsby & Kohlstedt, 1997, 2001; Qi et al., 2017; Treverrow et al., 2012). Recently, Bons et al. (2018) demonstrated that $n = 4$ provides a better fit to ice velocity data across the Greenland ice sheet.

Table 2. Parameters of Glen's flow law, Durham's flow law, and Goldsby-Kohlstedt composite flow law

Name of flow law	Creep regime	n	p	T, Temperature	A, material-dependent parameter	Q (activation energy, kJ/mol) or H (activation enthalpy, kJ/mol)
Glen's flow law	N/A	3	N/A	$T \geq 263K$	1.73×10^{21} ($MPa^{-3}s^{-1}$)	Q = 139
				$T < 263K$	3.61×10^{5} ($MPa^{-3}s^{-1}$)	Q = 60
Durham's flow law	N/A	4	N/A	$T \geq 243K$	$10^{11.8}$ ($MPa^{-4}s^{-1}$)	H = 91
Goldsby-Kohlstedt flow law	Dislocation	4	0	$T > 262K$	6.0×10^{28} ($MPa^{-4}s^{-1}$)	Q = 181
				$T < 262K$	5.0×10^{5} ($MPa^{-4}s^{-1}$)	Q = 60
	GBS-limited	1.8	1.4	$T > 262K$	3.0×10^{26} ($MPa^{-1.8}m^{1.4}s^{-1}$)	Q = 192
				$T < 262K$	3.90×10^{-3} ($MPa^{-1.8}m^{1.4}s^{-1}$)	Q = 49

2.3.2 Mechanical response due to evolving grain size

From experiments performed on fine-grained water ice, Goldsby & Kohlstedt (2001) proposed a composite flow law in which the total strain rate, $\dot{\varepsilon}_{total}$ arises from the strain rate contributions of four distinct creep mechanisms: (1) diffusion creep, $\dot{\varepsilon}_{diff}$, (2) grain boundary sliding (GBS) rate-limited by basal slip, $\dot{\varepsilon}_{basal}$, (3) basal slip rate-limited by GBS, $\dot{\varepsilon}_{GBS}$, and (4) dislocation creep, $\dot{\varepsilon}_{disl}$:

$$\dot{\varepsilon}_{total} = \dot{\varepsilon}_{diff} + \left(\frac{1}{\dot{\varepsilon}_{basal}} + \frac{1}{\dot{\varepsilon}_{GBS}}\right)^{-1} + \dot{\varepsilon}_{disl} \tag{5}$$

The term $\left(\frac{1}{\dot{\varepsilon}_{basal}} + \frac{1}{\dot{\varepsilon}_{GBS}}\right)^{-1}$ represents the serial operation of basal slip and GBS as accommodation mechanisms—the slower of these two processes limits their combined strain rate. Goldsby (2006) suggests that at temperatures warmer than 220 K and stresses greater than 10^{-4} MPa, $\dot{\varepsilon}_{diff}$ and $\dot{\varepsilon}_{basal}$ will be negligible. Thus, we can apply the composite flow law in a simplified form:

$$\dot{\varepsilon}_{total} = \dot{\varepsilon}_{disl} + \dot{\varepsilon}_{GBS} \tag{6}$$

Dislocation creep is a grain size insensitive mechanism described by a constitutive equation of the form shown in Eq. (4). GBS, on the other hand, is a grain size sensitive mechanism:

$$\dot{\varepsilon} = A\sigma^{n}d^{-p}\exp\left(-\frac{Q}{RT}\right), \tag{7}$$

where d is the grain size (m), p is the grain-size exponent. Goldsby & Kohlstedt (1997, 2001) derived $n = 4$ for dislocation creep (at high stresses) and $n = 1.8$ for GBS (at low stresses) and proposed that Glen's law ($n \approx 3$) arises from roughly equal contributions of dislocation creep and GBS at intermediate stresses. Recent glaciological modelling by Behn et al., (2020) likewise suggests that combined dislocation creep and GBS produces an effective stress exponent of $n = 3$ for ice sheets. We use the simplified composite flow law (Eq. (6)) to estimate ice strength evolution arising from grain size evolution, using the revised composite flow law parameters provided by Kuiper et al. (2020a, 2020b) (Table 2).

2.3.3 Mechanical response due to evolving CPO

To account for evolving viscous anisotropy (and enhancement) due to CPO development, Azuma (1994, 1995) developed a power law model that describes the creep strength of polycrystalline ice as a function of the total shear stress resolved onto (weak) ice basal planes. Azuma's flow law introduces the parameter S_{mean}—a scalar term which represents the mean reduced basal Schmid factor, *S*, for a given grain population (polycrystalline sample, in this case). For a given crystallographic orientation, the reduced basal Schmid factor reflects the shear stress resolved onto the basal plane (i.e., the easy glide plane), but does not consider the shear stress resolved along particular Burgers vectors (slip directions) lying within that plane. Thus, S_{mean} can be considered a proxy for the total shear stress resolved on ice basal planes during deformation. Azuma's flow law takes a similar form to that given in Eq. (4):

$$\dot{\varepsilon} = B\sigma^n \exp\left(-\frac{Q}{RT}\right) \tag{8}$$

However, the pre-exponential term, B ($MPa^{-n}s^{-1}$) follows a power law relationship with S_{mean} (see Fig. 9 from Azuma, 1995):

$$B \propto {S_{mean}}^{q}, q \approx 4 \tag{9}$$

such that, at a given stress, a sample with greater resolved shear stresses on the ice basal planes (i.e., larger S_{mean}) will deform faster; conversely, at a given strain rate, a sample with larger S_{mean} will deform at a lower stress.

A key assumption of Azuma (1994, 1995) is that, under their experimental conditions—relatively low temperatures (-10 to -20 °C), low strain rates (~2×10^{-7} to $4 \times 10^{-7} s^{-1}$), and low strains (~5.7%)—dynamic recrystallization should be negligible. Therefore, all strain weakening measured in their experiments could be attributed to CPO development. However, Azuma (1995) observed that for a given value of S_{mean}, small variations in B could be attributed to differences in grain size, impurity content, and grain shape among different experimental studies. In this study, we place upper and lower bounds on B—B_{upper} and B_{lower}, respectively—for each S_{mean} value, following Fig. 9 from Azuma (1995).

$$\begin{gathered} log_{10}(B_{upper}) = 4.2 \cdot log_{10}(S_{mean}) + 8 \\ log_{10}(B_{lower}) = 4.8 \cdot log_{10}(S_{mean}) + 7.4 \end{gathered} \tag{10}$$

2.4. Model input data

To reiterate, we use grain sizes and *c*-axis orientations calculated from EBSD maps (Sect. 2.2) of ice samples deformed to successively higher strains (Sect. 2.1) as an input to the constitutive relationships described above (Sect. 2.3). These microstructural measurements along with the experimental boundary conditions (temperature, stress, and/or strain rate) are substituted into the mechanical models (Sect. 2.3) to constrain the contributions of grain size evolution and/or CPO development to strain weakening.

2.4.1 Grain size

Grain size is defined here as the diameter of a circle with an area equal to the measured area of each grain (i.e., area-equivalent diameter). We use both median grain size, and the full grain size distribution of each sample, as an input into the composite flow law Eq. (6). Median grain sizes have been shown to most accurately reflect the "average" grain size of right-skewed and lognormal grain size distributions (Lopez-Sanchez, 2020; Ranalli, 1984) like those observed in our samples (Fan et al., 2020; Fan et al., 2021a).

To model ice strength evolution using the full grain size distributions, we firstly estimate the volume fraction of different grain size classes using the Scheil-Schwartz-Saltikov method (Saltikov, 1967; Scheil, 1931; Schwartz, 1934) (technical details in Appendix B). For polycrystalline materials, aggregate strength falls between two end-member bounds: (1) a homogeneous stress bound (Sachs bound), with local strain rate varying from grain to grain, and (2) a homogeneous strain rate bound (Taylor bound), with local stress varying from grain to grain (Freeman & Ferguson, 1986; Ter Heege et al., 2004). In reality, aggregate strength probably falls between these end-member bounds. To place upper and lower bounds on sample strength evolution, we therefore calculate both the Sachs (homogeneous stress) and Taylor (homogeneous strain rate) limits for both the constant displacement rate and constant load experiments (details in Appendix C). It is worth noting here that the composite flow law (Goldsby & Kohlstedt, 1997, 2001), which we use to model grain size effects, was derived from fine-grained (< 100 μm) ice samples deformed at low temperatures (≤ -25 °C), to low strains (mostly ≤ 3%). We assume that Goldsby & Kohlstedt's samples did not undergo significant grain size reduction under their experimental conditions, meaning that the composite flow law should not already incorporate implicit grain size distribution effects.

2.4.2 Crystallographic preferred orientation (CPO)

For each sample in this study, the *c*-axis orientations calculated from the EBSD data (one point per pixel) were applied to estimate the resolved shear stress on the crystallographic basal plane. For each pixel, the resolved shear stress on ice basal plane can be quantified by a reduced Schmid factor, S (e.g., Azuma, 1995). Under uniaxial compression, where the compression direction is parallel to the sample shortening axis (Fig. 1(a)), S can be calculated from the angle (θ) between each *c*-axis measurement and the compression axis (Eq. (11).

$$S = \frac{\sin(2\theta)}{2} \tag{11}$$

S, is the highest (with the value of 0.5) for the *c*-axis at 45° to the compression direction, and it decreases to zero as the *c*-axis becomes parallel or perpendicular to the compression direction (Fig. 1(b)).

The number frequency of *c*-axes observed from a 2-D surface is impacted by a stereological issue that, in turn, biases reduced Schmid factor measurements. Namely, for a random orientation distribution, *c*-axes lying sub-normal to the compression direction ($\theta \approx 90°$) are much more abundant than *c*-axes lying sub-parallel to the compression direction ($\theta \approx 0°$) (see Fig. 1(c), green histogram). This effect arises because the area of a stereoplot lying between two "co-latitudes" (i.e., small circles) of fixed separation (e.g., 10°) increases with increasing angle (θ) from the stereoplot centre (origin) (Fig. 1(b)). For a random population of *c*-axis orientations, this effect produces a reduced Schmid factor frequency distribution that is strongly biased towards high reduced Schmid factors (purple histogram, Fig. 1(c)). On the other hand, for a random orientation distribution, the densities (number frequency per unit area) of c-axes lying between two co-latitudes of fixed separation should be the same (Fig. 1(d); details for the calculation of c-axis densities are in Appendix D). Consequently, there should be a uniform density distribution of reduced Schmid factors for a random orientation distribution (Fig. 1(d)). Therefore, for a given orientation distribution comprising m classes of reduced Schmid factors (S_1, S_2, S_3, …, S_m) and number frequency densities (Φ_1, Φ_2, Φ_3, …, Φ_m), we can estimate the bulk reduced Schmid factor, S_{bulk}, following:

$$S_{bulk} = \frac{\Phi_1\bar{S}_1 + \Phi_2\bar{S}_2 + \Phi_3\bar{S}_3 + \cdots + \Phi_m\bar{S}_m}{\Phi_1 + \Phi_2 + \Phi_3 + \cdots \Phi_m}, \qquad (12)$$

where $\bar{S}_1$, $\bar{S}_2$, $\bar{S}_3$, …, $\bar{S}_m$ are the mean values of reduced Schmid factor in each class. In this study, we use 100 classes (bins) of reduced Schmid factors (i.e., $m = 100$; Schmid factor interval of 0.005). Undeformed fine-grained and median-grained ice samples have S_{bulk} of ~0.24 (Tables 3(a, b)), and they are very close to a random CPO (S_{bulk} = 0.25). The ice mechanical behaviours estimated from the Azuma's flow law with the input of bulk reduced Schmid factor, S_{bulk} (Eq. (12)) and the number weighted mean reduced Schmid factor ($\bar{S} = \frac{1}{N}\sum S$) are similar (full details provided in Sect. S1 of supplement). We choose to use estimations from the bulk reduced Schmid factor, S_{bulk}, in the following discussions.

Table 3(a). Summary of measured and estimated strain rate for experiments with constant load at -4 °C

Large table presented at the end of this manuscript as well as in a separate spreadsheet.

Table 3(b). Summary of measured and estimated stress for experiments with constant displacement rate at -10 °C

Large table presented at the end of this manuscript as well as in a separate spreadsheet.

Table 3(c). Summary of measured and estimated bulk stress for undeformed sample and uniaxial compression experiments with constant displacement rate at -30 °C

Large table presented at the end of this manuscript as well as in a separate spreadsheet.

2.5 Normalisation of measured and modelled bulk strain rate/stress

To assess how well each model reproduces the measured (experimental) mechanical data, we need to examine both (1) the absolute magnitude of the stresses and strain rates predicted by each model and (2) the "patterns" of strain weakening predicted by each model—that is, the relative amount (percentage) of strain weakening predicted by each model, and the predicted strains required to reach steady-state conditions. To make it easier to assess the patterns of strain weakening predicted by each model, we normalise the modelled and measured stresses (for constant displacement rate experiments) and strain rates (for constant load experiments) by their values at the strain corresponding most closely to the peak stress and minimum strain rate, respectively. This method is similar to that applied by Jacka & Li, (2000) and enables us to make a more direct comparison between the patterns of strain weakening predicted by each model, while also removing sample-to-sample variability. Meanwhile, the unnormalized data are used to assess how well each model reproduces the absolute measured stress and strain rate magnitudes. The unnormalized and normalized mechanical data are summarized for each sample in Tables 3(a-c).

Constant load experiments

For each experimental run with constant load, the measured strain rate-strain curves are normalised with respect to the minimum strain rate following:

$$\bar{\dot{\varepsilon}}_{measure} = \frac{\dot{\varepsilon}_{measure}}{\dot{\varepsilon}_{min,measure}}, \tag{13}$$

where $\bar{\dot{\varepsilon}}_{measure}$ is the normalised measured strain rate, $\dot{\varepsilon}_{min,measure}$ is the measured minimum strain rate at ~1-2% strain.

Modelled uniaxial strain rates were normalised following:

$$\bar{\dot{\varepsilon}}_{model} = \frac{\dot{\varepsilon}_{model}}{\dot{\varepsilon}_{1\%,model}}, \tag{14}$$

where $\bar{\dot{\varepsilon}}_{model}$ is the normalised modelled strain rate, $\dot{\varepsilon}_{model}$ is the modelled strain rate corresponding to the maximum strain of each sample, $\dot{\varepsilon}_{1\%,model}$ is the modelled strain rate at the strain of ~1%.

Constant displacement rate experiments

For each experimental run with constant displacement rate, the measured stress-strain curves are normalised with respect to the peak stress following:

$$\bar{\sigma}_{measure} = \frac{\sigma_{measure}}{\sigma_{peak,measure}}, \tag{15}$$

where $\bar{\sigma}_{measure}$ is the normalised measured stress, $\sigma_{peak,measure}$ is the measured uniaxial stress at ~2-3% strain. The decrease of normalised measured stress relative to the peak, $\Delta\bar{\sigma}_{measure}$, is:

$$\Delta\bar{\sigma}_{measure} = 1 - \bar{\sigma}_{measure} \tag{16}$$

Modelled stresses are normalised for ice samples deformed under the same temperature and similar strain rates following:

$$\bar{\sigma}_{model} = \frac{\sigma_{model}}{\sigma_{3\%,model}}, \tag{17}$$

where $\bar{\sigma}_{model}$ is the normalised modelled stress, σ_{model} is the modelled stress corresponding to the maximum strain of each sample, $\sigma_{3\%,model}$ is the modelled stress at the strain of ~3%. At each finite strain, the decrease of normalised modelled stress relative to 3% strain, $\Delta\bar{\sigma}_{model}$, is:

$$\Delta\bar{\sigma}_{model} = 1 - \bar{\sigma}_{model} \tag{18}$$

3. Results

3.1 Measured mechanical data

3.1.1 Constant load experiments

The measured strain rate, $\dot{\varepsilon}_{measure}$, and normalised strain rate, $\bar{\dot{\varepsilon}}_{measure}$, are plotted as a function of strain in Figs. 2(a-c) and 3(a-c), respectively (black curves). Measured and normalised strain rates initially decrease with strain before reaching a minimum at ~1–2% shortening. After that, deformation accelerates (strain rate increases) until a near-constant, steady-state strain rate is reached at around $\varepsilon =$ ~6%. However, in many experiments there is a slight strain rate decrease beyond $\varepsilon =$ ~8%. Meanwhile, stress decreases continuously, albeit modestly, during each constant load experiment, due to an increase in sample cross-sectional area (black line, Fig. 2(d); Eq. (3)).

3.1.2 Constant displacement rate experiments

Measured stresses are plotted as a function of strain in Figs. 2(e-g), 2(i-k) and 2(m-o) (black curves). Stress initially increases as a function of strain, reaching a peak at strains of 1–3%. Thereafter, stress drops 31–38% until a flow stress is reached by ~20% shortening (black curves, Figs. 3(e-g), 3(i-k) and 3(m-o); black dots, Figs. 3(h, l, p); Tables 3(b, c)). In general, both peak and flow stresses increase with increasing strain rate and decreasing temperature. Strain rate increases modestly through each constant rate experiment as a result of continuous sample shortening (black lines, Figs. 2(h), 2(l), 2(p); Eq. (2)).

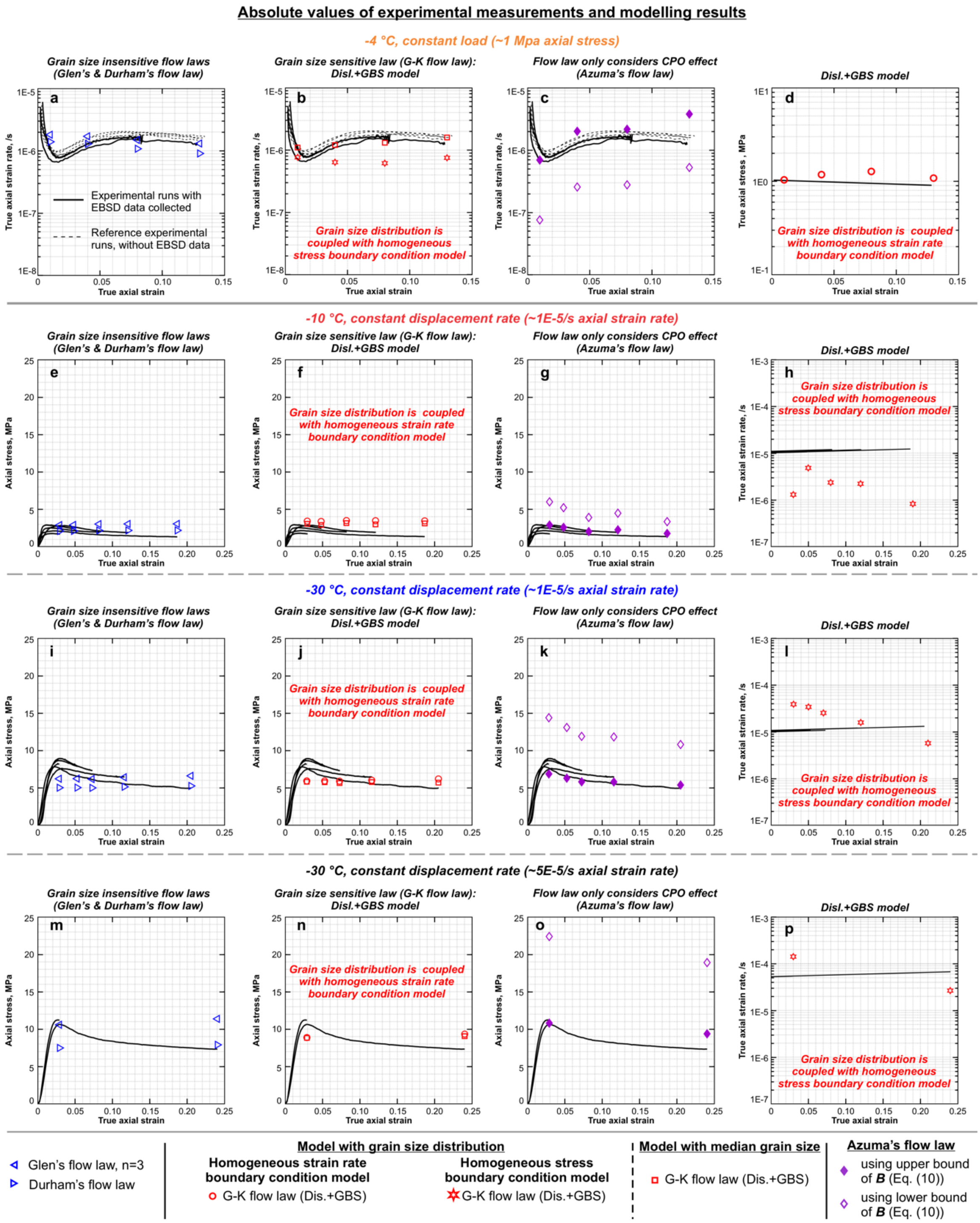

Figure 2. Comparing the absolute values of measured and modelled mechanical data for experiments under conditions of: **(a)–(d)** constant load ($\boldsymbol{\sigma} = \sim 1$ MPa), $\boldsymbol{T}$ = -4 °C; (e)–(h) constant displacement rate ($\dot{\boldsymbol{\varepsilon}} = \boldsymbol{\sim 1 \times 10^{-5} s^{-1}}$), $\boldsymbol{T}$ = -10 °C; (i)–(l) constant displacement rate ($\dot{\boldsymbol{\varepsilon}} = \boldsymbol{\sim 1 \times 10^{-5} s^{-1}}$), $\boldsymbol{T}$ = -30 °C; **(m)–(p)** constant displacement rate ($\dot{\boldsymbol{\varepsilon}} = \boldsymbol{\sim 5 \times 10^{-5} s^{-1}}$), $\boldsymbol{T}$ = -30 °C. Mechanical data from experimental measurements are coloured black; Modelled mechanical data are coloured non-black. Modelling results using mechanical models without considering microstructural evolutions (Sect. 2.3.1) are illustrated in **(a)**, **(e)**, **(i)** and **(m)**. Modelling results using the mechanical model that considers grain size effects (Sects. 2.3.2) are shown in **(b)**, **(f)**, **(j)** and **(n)**. Modelling results using the mechanical model that considers CPO effects (Sect. 2.3.3) are shown in **(c)**, **(g)**, **(k)** and **(o)**. When grain size distribution is considered during the modelling, homogeneous stress deformation boundary condition model (Sect. 2.4.1; Appendix C) is applied to estimate the strain rate from the measured stress (**(a)–(c)**, **(h)**, **(l)**, **(p)**); homogeneous strain rate deformation boundary condition model (Sect. 2.4.1; Appendix C) is applied to estimate the stress from the measured strain rate (**(d)**, **(e)–(g)**, **(i)–(k)**, **(m)–(o)**).

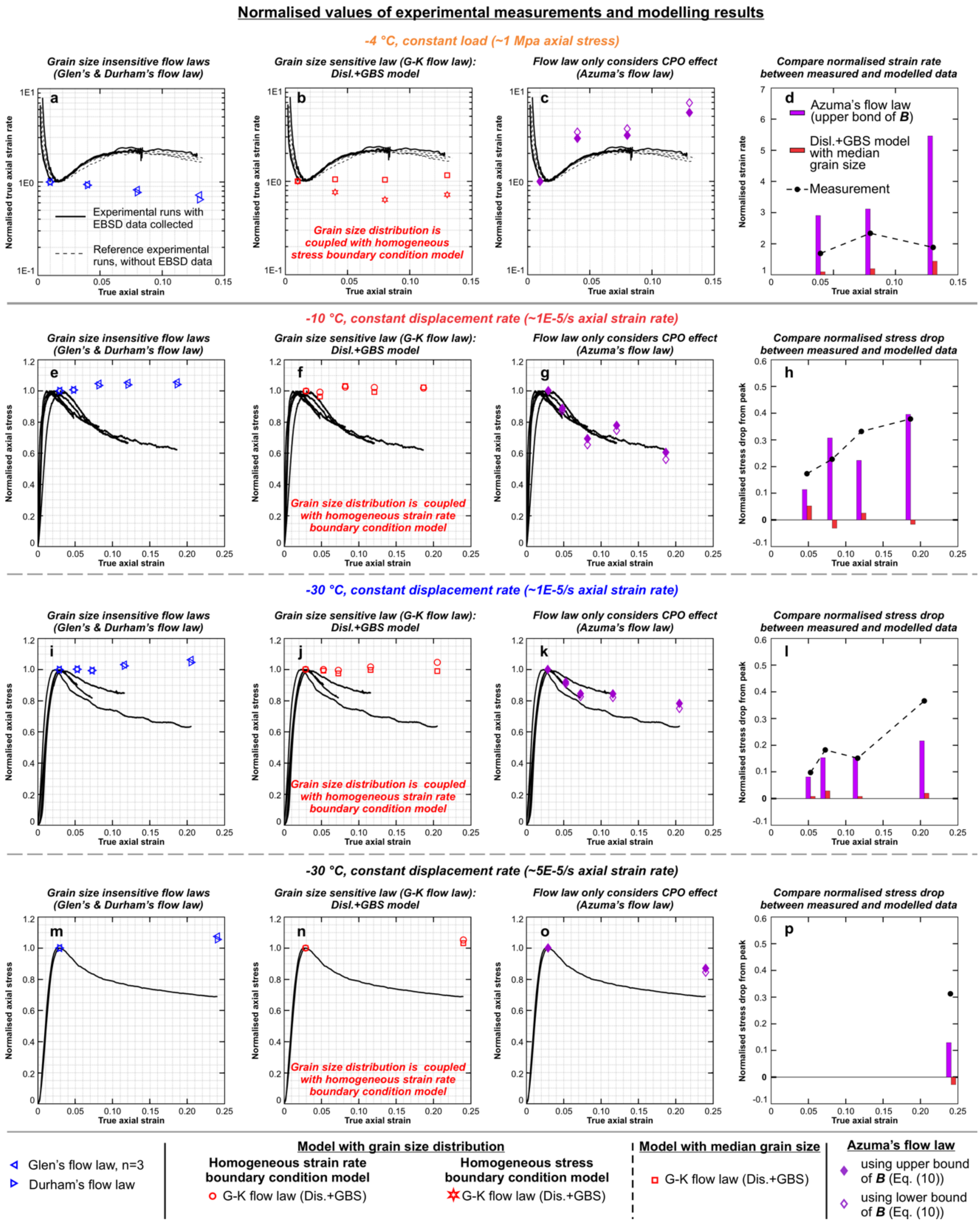

Figure 3. Comparing the normalised values (Sect. 2.5) of measured mechanical data (coloured black) and modelled mechanical data (coloured non-black). The deformation conditions for each row are the same as in Fig. 2. For the first three columns, the mechanical models used for modelling are the same as Fig. 5. **(d)** Comparing the measured normalised strain rate (Eq. (13); coloured black) with the modelled normalised strain rate (Eq. (14)) using the Dislocation+GBS model (coloured red) or the Azuma's flow law (coloured purple). **(h)**, **(l)**, **(p)** Comparing the measured normalised stress drop (Eq. (16) (coloured black) with the modelled normalised stress drop (Eq. (18) using the Dislocation+GBS model (coloured red) or the Azuma's flow law (coloured purple).

3.2 Microstructures

The microstructures of these samples have been described in detail in Fan et al. (2020, 2021a). We will summarise the pertinent observations here, but the reader can refer to Fan et al. (2020, 2021a) for the full details.

3.2.1 Grain size

At all temperatures with strains higher than ~3%, larger grains with more irregular grain boundaries interlock with finer grains with less irregular grain boundaries (Fig. 4(a)−6(a)). Samples deformed at -30 °C to strains of $\varepsilon \geq$ ~12% show a "core-and-mantle" structure (Gifkins, 1976; White, 1976), characterised by a "necklace" of finer grains encircling larger grains (Fig. 9(a)).

With increasing strain over all temperatures (-30 to -4 °C), the number frequency of fine grains (in general smaller than ~150 μm) become more abundant at the expense of large grains (in general larger than ~150 μm) (Figs. 4(b)−6(b)), leading to a modest decrease in median grain sizes (Figs. 4(b)−6(b); Tables 1(a, b)). However, fine grains become volumetrically dominant only at large strains (≥ 12%) in the lowest temperature (i.e., -30 °C) samples (Fig. 6(c)). In all other samples, large grains occupy a much greater volume of each sample (Figs. 4(c)−6(c)).

3.2.2 Crystallographic preferred orientations (CPOs) and reduced Schmid factors

For samples deformed at -4 and -10 °C, the CPOs are close to random at strains of $\varepsilon <$ ~3% (Figs. 4(d, e), 5(d, e)). The CPO becomes clearer at $\varepsilon >$ ~4%, with c-axes preferentially aligned in a cone (small circle) centred around the compression axis (Figs. 4(d), 5(d)). Accordingly, the number frequency density (Φ, Sect. 2.4.2) of c-axes at θ of 30−50° increases (relative to the undeformed starting material) whilst Φ decreases for c-axes at θ = 0−30° and 50−90°—this change becomes more marked with increasing strain (Figs. 4(e), 5(e), gold histograms). For samples deformed at -30 °C, the CPO is close to random at $\varepsilon \leq$ ~5% (Figs. 6(d, e)). However, with increasing strain ($\varepsilon \geq$ ~8%), c-axes form a tight cone around the compression axis, increasing the number frequency density of c-axes at 0−45°, relative to those at 45−90° (Fig. 6(e), gold histograms). The c-axis cone becomes tighter with increasing strain, until it becomes a broad cluster at ~20% strain (Fig. 6(d)).

In all samples with $\varepsilon \geq$ ~5%, the number frequency density of measurements with $S > 0.4$ increases with strain, whilst the Φ of measurements with $S < 0.4$ decreases with strain (Figs. 4(f)−6(f)). This trend is more pronounced at -4 and -10 °C than at -30 °C (compare Figs. 4(f), 5(f) with Fig. 6(f)). As a result, the bulk reduced Schmid factor, S_{bulk}, generally increases with increasing strain at both high and low temperatures; however, at any given strain, S_{bulk} is lower at lower temperatures (Tables 3(a-c)).

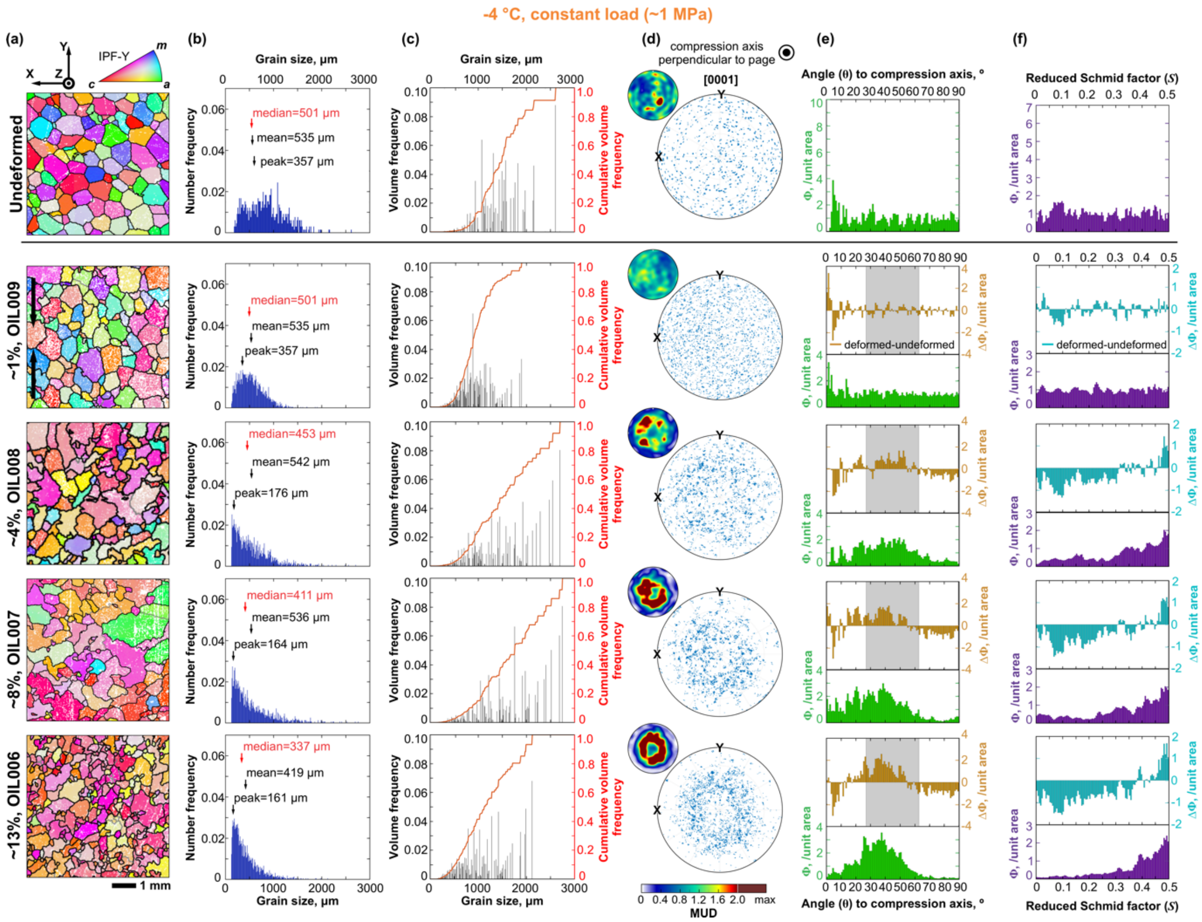

Figure 4. Microstructural analyses of deformed ice samples at -4 °C under uniaxial compression with constant load ($\boldsymbol{\sigma}$ = ~1 MPa). The EBSD data are presented as **(a)** orientation maps. Orientation maps are coloured by IPF-Y, which uses the colour map to indicate the crystallographic axes that are parallel to the vertical shortening direction as shown by the black arrows. Ice grain boundaries with a misorientation larger than 10° are shown black. Non-indexed pixels are shown white. Subgrain boundaries, where misorientation angles between neighbouring pixels are between 2° and 10°, are shown grey. Maps show data without interpolation. **(b)** Grain size distribution with a bin width of 10 μm for each grain size class. Mean and peak grain sizes are indicated by black arrows. Median grain size is indicated by a red arrow. **(c)** Bar plots (grey) show estimated volume frequency for each grain size class (Sect. 2.4.1; Appendix B). Red curves show the cumulative volume frequency as a function of grain size. **(d)** The distributions of *c*-axes orientations in stereonet with one point per pixel; they are displayed as point plots (with 5000 randomly selected points). The point plots are also contoured by multiples of a uniform distribution (MUD) with a half-width of 7.5°. **(e)** Green bars represent the number frequency density ($\boldsymbol{\Phi}$; Sect. 2.4.2; Appendix D) of *c*-axes at different angles to the compression axis ($\boldsymbol{\theta}$) with an interval of 0.1°. Yellow bars represent the differences of $\boldsymbol{\Phi}$ for *c*-axes between each deformed sample and the undeformed sample at each $\boldsymbol{\theta}$ interval. The grey area marks the range of $\boldsymbol{\theta}$ that corresponds to high reduced Schmid factors ($\boldsymbol{S}$> 0.4; Fig. 1(b)). **(f)** Purple bars represent the number frequency density ($\boldsymbol{\Phi}$) of *c*-axes at different reduced Schmid factors (S) with an interval of 0.005. Blue bars represent the differences of $\boldsymbol{\Phi}$ for *c*-axes between each deformed sample and the corresponding undeformed sample at each S interval.

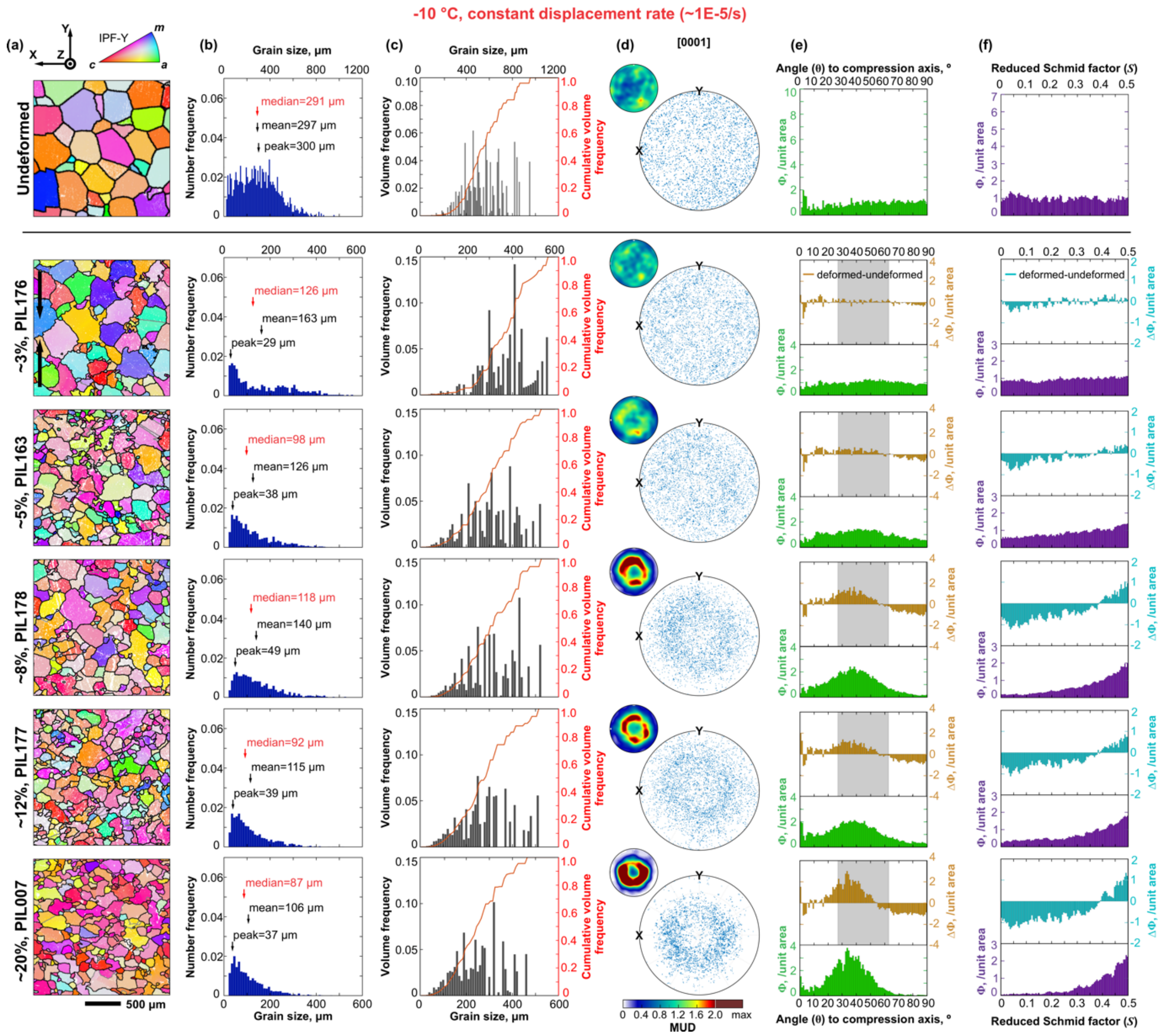

Figure 5. Microstructural analyses of deformed ice samples at -10 °C under uniaxial compression with constant displacement rate ($\dot{\boldsymbol{\varepsilon}} = \sim\mathbf{1} \times \mathbf{10^{-5}} \boldsymbol{s^{-1}}$). The descriptions of columns **(a)–(f)** are the same as Fig. 4.

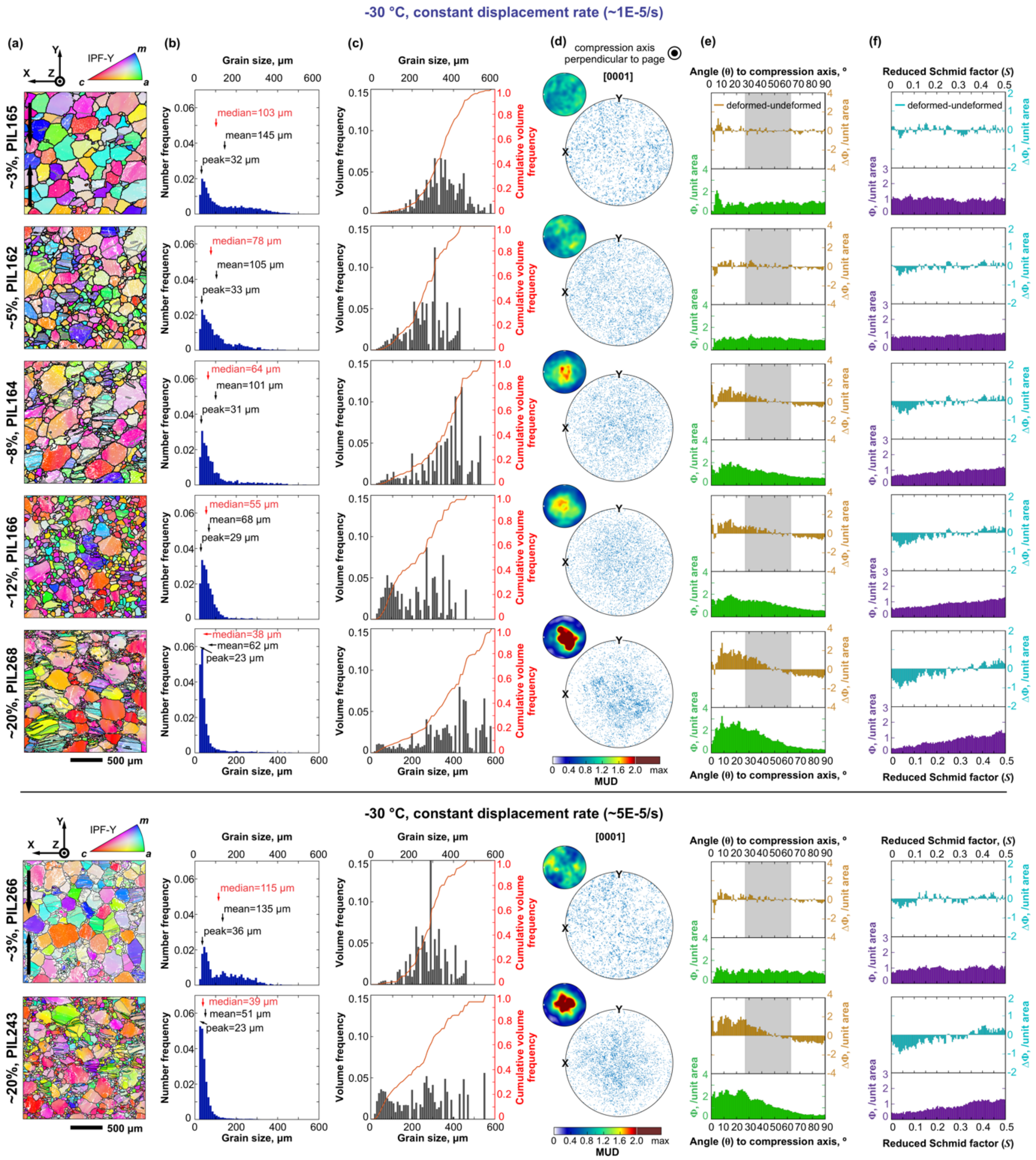

Figure 6. Microstructural analyses of deformed ice samples at -30 °C under uniaxial compression with constant displacement rate ($\dot{\boldsymbol{\varepsilon}} = \boldsymbol{\sim 1 \times 10^{-5}}$ or $\boldsymbol{\sim 5 \times 10^{-5} s^{-1}}$). The descriptions of columns **(a)–(f)** are the same as Fig. 4.

3.3 Ice strength evolution models

As described above (Sects. 2.3, 2.5), we compare the magnitude (absolute value; Fig. 2) and pattern (normalised value; Fig. 3) of ice strength evolution between experimental measurements (black curves) and modelling results (coloured symbols). For experiments conducted at similar conditions (temperature, stress/strain rate), we model the evolution of strain rate and/or stress as a function of strain and microstructural evolution (grain size, CPO) using:

(1) Ice flow laws that do not consider grain size or CPO effects (Durham et al., 1983; Glen, 1955) (blue symbols, first column in Figs 2 and 3).

(2) An ice flow law that incorporates grain size sensitivity (Goldsby & Kohlstedt, 1997, 2001). We account for grain size evolution using both median grain sizes (red squares, second column in Figs 2 and 3) and the full measured grain size distributions. For models that use the full grain size distribution, we calculate both the isostress (Sachs) limit (red circles) and isostrain (Taylor) limit (red stars).

(3) An ice flow law that accounts only for CPO development (Azuma, 1994, 1995) (purple symbols, third column in Figs 2 and 3).

Note again that strain weakening is represented by a bulk strain rate increase after the strain rate minimum for constant load experiments (first row in Figs 2 and 3), and it is represented by a bulk stress decrease after the peak stress in constant displacement rate experiments (second, third, and fourth row in Figs 2 and 3). Therefore, to evaluate the pattern (i.e., normalised value) of strain weakening, we compare the normalised strain rates for constant load experiments; we compare the normalised stress for constant displacement rate experiments (Fig. 3).

3.3.1 The magnitude (absolute value) of strain rate or stress

At all conditions, all the mechanical models (coloured symbols, Figs 2 and 3) predict ice strengths within an order of magnitude of those measured experimentally (black curves, Figs 2 and 3). For the model that considers grain size effects, the models using median grain sizes and grain size distributions provide similar results (red symbols, second column in Fig. 2), which in turn are very similar to the microstructure-insensitive (Glen, Durham) models (compare first and second columns in Fig. 2). Both types of models predict strain rates that lie between the measured secondary minimum and tertiary maximum strain rates for constant load experiments (Figs. 2(a, b)), and stresses that lie between the measured peak and flow stresses for constant displacement rate experiments (Figs. 2(e-f, i-j, m-n)). For the (Azuma) model that considers CPO effects, the strain rates (for constant load experiments) and stresses (for constant displacement rate experiments) predicted using the upper bound of the pre-exponential term, *B* (Eq. (8), Sect. 2.3.3) lie very close to the experimental measurements (Figs. 2(c, g, k, o)).

3.3.2 The pattern (normalised value) of strain rate or stress

Mechanical models that do not consider microstructural evolution (coloured blue) as well as the mechanical model that considers grain size effects, i.e., Dislocation+GBS model (coloured red) estimate that sample strength does not evolve significantly as a function of strain (Figs. 3(a-b, e-f, i-j, m-n)). Such modelled pattern does no match experimental measurements—normalised strain rate increases with strain after secondary minimum (under constant load); normalised stress decreases with strain after peak stress (black curve, Fig. 3).

Meanwhile, Azuma's CPO model closely matches the measured magnitudes of strain weakening in most cases (Figs. 3(c, g, k, o)). However, Azuma's model overestimates the strain rate increase under constant load conditions (at -4°C) by a factor of ~3 (Figs. 3(c, d)) and underestimates the stress drop magnitude by a factor of ~2 under constant displacement rate conditions at -30°C and ~5E-5/s strain rate (Figs. 3(o, p)).

4. Discussion

4.1 Measured mechanical data and deformation mechanisms

4.1.1 Measured mechanical data

Under constant load, the strain rate-strain curves (coloured black, Figs. 2(a-c), Sect. 3.1.1) and the enhancement factor values of ~2 (ratio between the strain rate at strains of $\varepsilon \geq 8\%$ and the minimum strain rate) (Table 3(a), Fig. 3(d)) generally match published constant load experiments (Budd & Jacka, 1989; Jacka & Li, 2000).

Under constant displacement rate, the stress-strain curves (black curves, Fig. 2, Sect. 3.1.2) and the percentage of stress-drop from peak (~31−38%) at 20% strain (Tables 3(b, c), Figs. 3(h, l, p)), and it has no apparent correlations with temperature or strain rate. This observation matches published experiments that cover a much wider temperature and/or strain rate ranges (Sect. S2 of the supplement; Durham et al., 1983, 1992; Piazolo et al., 2013; Qi et al., 2017; Vaughan et al., 2017).

4.1.2 Deformation and recrystallization mechanisms

The microstructures and deformation mechanisms in these samples have been discussed in detail elsewhere (Fan et al., 2020, 2021a). To summarize those papers, these samples undergo:

(1) At high temperatures (≥ -10°C), samples exhibit microstructures characteristic of rapid grain boundary migration, which favours the competitive growth of grains in easy slip orientations (*c*-axes at ~45° to compression), leading to the formation of cone-shaped *c*-axis CPO centred around the compression direction (Figs. 4(d), 5(d)).

(2) Dynamic recovery leads to the progressive development of intragranular (subgrain) boundaries (coloured grey, Figs. 4(a)–6(a)).

(3) With increasing strain, small recrystallized grains nucleate at the expense of large, original grains, forming a core-and-mantle structure with fine-grained networks of recrystallized grains. Recrystallized grains have much weaker CPOs than their neighbouring parent grains, suggesting that grain nucleation occurs via either (1) subgrain rotation recrystallization followed by grain boundary sliding that randomizes the CPO, or (2) spontaneous nucleation of fine grains in random orientations.

(4) As temperature decreases, lattice rotation (due to dislocation glide on the basal plane) becomes increasingly important. Basal planes progressively rotate into the compression-normal plane, producing a *c*-axis cluster or narrow-cone around the compression axis particularly at low temperatures, ≤ -20°C (Figs. 6(d)).

(5) All the deformed samples have a major volume frequency peak corresponding to the large, original grains (Fig. 4(c)–6(c)). A secondary volume frequency peak at finer sizes (corresponding to recrystallized grains) only becomes obvious at -30 °C with high strains (Fig. 6(c)). Recrystallized grains are therefore volumetrically insignificant for most of the ice samples analysed in this study.

4.2 Contributions of microstructural evolution to strain weakening

The stresses and strain rates predicted by all the mechanical models generally match the experimental measurements in magnitude (Fig. 2; Sect. 3.3.1), indicating that they provide a certain level of reliability in the estimation of ice strength, at least under laboratory conditions. These data as well as the normalised data further show that the experimentally measured strain weakening (black curves, Figs. 2, 3; Sect. 4.1.1) cannot be predicted by mechanical models that do not consider microstructural changes (blue symbols, Fig. 3). Thus, to accurately quantify strain weakening and enhancement in glaciers and ice sheets, it is necessary to account for the evolving microstructural state of ice.

4.2.1 Grain size reduction

Under all conditions, the median grain size and grain size distribution of each sample shifts towards finer grain sizes with increasing strain, due to the nucleation of fine grains at the expense of large, original grains (Figs. 4(b)−6(b)). Intuitively, we would expect a strength decrease with decreasing grain size due to the activation of GBS. However, the Dislocation+GBS model does not predict any decrease in sample strength with increasing strain (red marks, Fig. 3). On the contrary, the grain size models show an increase in sample strength with increasing strain (e.g., Figs 2(f, j, n)) due to the modest increase in strain rate that arises from sample shortening. These models indicate that grain size has little impact on the strength of ice under the (high temperature, $T_h \geq 0.9$, relatively high stress, >1 MPa) conditions explored in this study. We suggest that grain size plays a negligible role in ice strength evolution here because even though fine grains become more abundant with increasing strain, their contribution to the total volume sample remains insignificant (Figs. 4(c)−6(c); Sect. 3.2.1). Consequently, the grain size sensitive component of bulk ice strength is governed by the volumetrically dominant, large, original grains, both at low and high strains.

The Dislocation+GBS model also predicts similar ice strength when incorporated with either median grain size or grain size distribution data (red marks, Fig. 2). These data suggest that predicting ice strength using a (simple) single value of median grain size is generally equivalent to using the (more sophisticated) grain size distribution.

It is worth noting that even though grain size reduction yields little influence over strain weakening at the experimental conditions explored here (compare red marks and black curves in Fig. 3), the composite flow law of Goldsby & Kohlstedt (1997, 2001) suggests that GBS still provides a significant contribution towards the deformation. To illustrate this, we plot deformation mechanism maps (grain size versus stress) for each temperature explored here, with strain rate contours calculated according to Goldsby & Kohlstedt (1997, 2001) (Fig. 7). On each map, the point representing stress-grain size data obtained from this study and published literatures (Fan et al., 2020; Jacka & Li, 1994; Jacka & Maccagnan, 1984; Vaughan et al., 2017) are superposed on the deformation mechanism maps. All of these data summarized in Table 4. Details of the processing of published data are summarized in Appendix E. Figure 7 shows that across a broad range of temperatures, stresses, and strain rates, the experimental stress-grain size data points all lie close to the deformation mechanism boundary (thick solid black line, Fig. 7), indicating roughly equal contributions of dislocation creep and GBS to the total strain rate. Moreover, for most of the data points, the ratio between the strain rates provided by dislocation creep and GBS is < 10; thus, in most of the samples examined here, GBS accommodates at least 10% of the total deformation. Figure 7 also demonstrates that for experiments performed under relatively high stresses (≥ 1 MPa), the stress-grain size data migrate from the dislocation creep regime towards the GBS-limited creep regime with increasing strain (Figs. 7(b-f)). At low stresses (~0.4 MPa) (Jacka & Maccagnan, 1984), on the other hand, the data points shift from the GBS-limited creep regime towards the dislocation creep regime with increasing strain (Fig. 7(a)). These trends indicate that grain size reduction dominates at high stresses, whereas grain growth dominates at low stresses. Thus, GBS becomes increasingly insignificant with increasing grain size at low stresses.

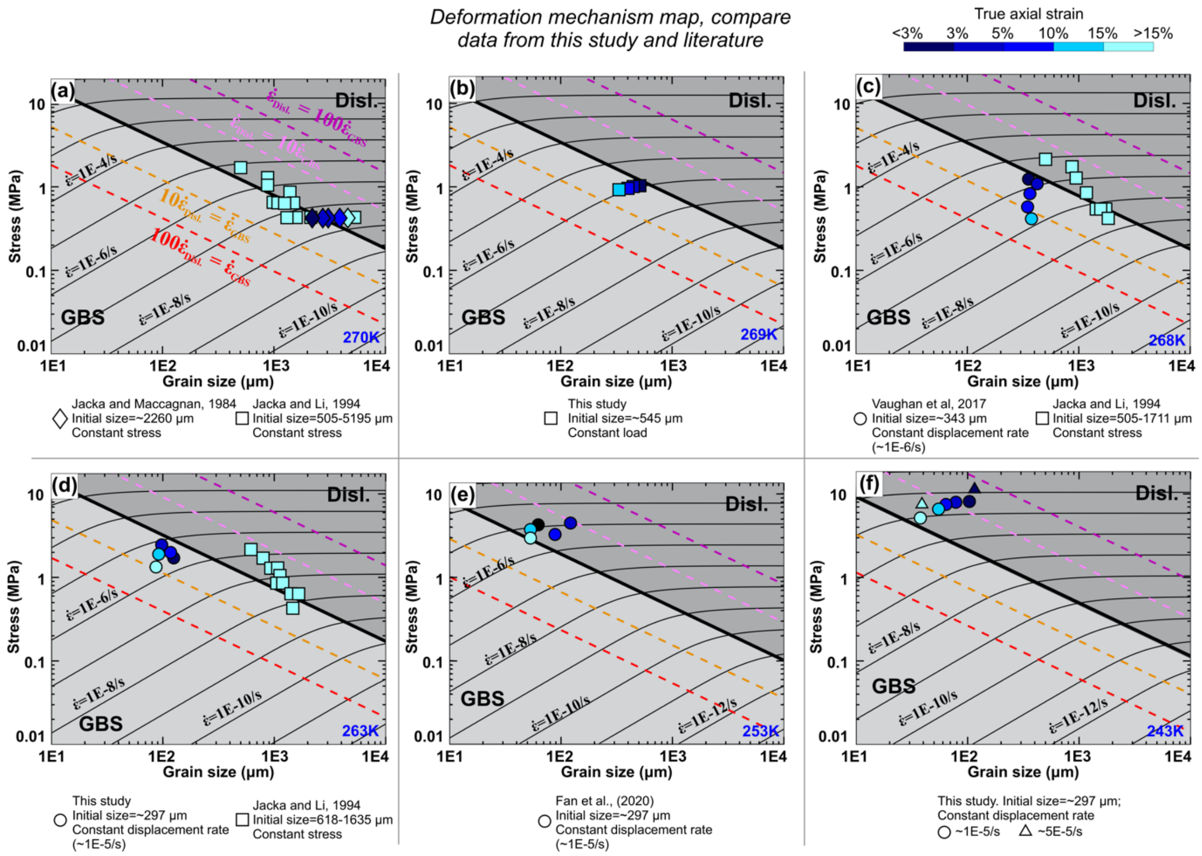

Figure 7. Deformation mechanism maps that display the relationship between the three macroscopic variables: stress (y-axis), grain size (x-axis) and strain rate (contours with thin black lines) at different temperatures. Strain rate contours are calculated using corresponding flow law parameters (Table 2, from Kuiper et al (2020a, 2020b)) for dislocation creep (Eq. (4)) and GBS-limited creep regime (Eq. (7)). Thick black solid line represents the deformation mechanism boundary, at where dislocation creep strain rate equals to GBS strain rate. Dashed coloured lines represent the ratio between the dislocation creep strain rate and the GBS strain rate. Points representing stress-grain size relationships using experimental data from this study and published literature (Jacka and Maccagnan, 1984; Jacka and Li, 1994; Vaughan et al., 2017; Fan et al., 2020) are superposed over deformation mechanism maps at different temperatures.

Table 4. Summary of strain rate, stress, and grain size of data from this study and the literature

Large table presented at the end of this manuscript as well as in a separate spreadsheet.

4.2.2 CPO development

The mechanical model that solely considers CPO effect (Azuma's flow law) predicts strain weakening across all conditions, manifested as a strain rate enhancement under constant load conditions, and a stress drop under constant rate conditions (compare purple marks and black curves in Figs. 2, 3), as observed in the experimental mechanical data. Moreover, at -10 and -30 °C with ~1E-5/s strain rate, the percentage of stress drop from peak stress predicted from the Azuma's flow law generally matches experimental measurements at each strain (Figs. 3(h, l)). Thus, all of the strain weakening observed in this study can be explained by CPO development.

At high temperatures (≥ -10°C), *c*-axes evolve towards a small circle (open cone) distribution around the compression axis (Figs. 4(d) and 5(d)), whereas at low temperatures (30°C), *c*-axes evolve towards a single cluster parallel with the compression axis (Figs. 6(d)). The cone-shaped *c*-axis alignment results from grains evolving towards easy slip orientations—i.e., *c*-axes inclined 30−60° from the compression axis (Fig. 4(e))—corresponding to high reduced Schmid factors of S = 0.4−0.5 (Figs. 4(f), 1(b)). Thus, cone CPO development should produce an increase in the bulk reduced Schmid factor, S_{bulk}, resulting in sample softening and strain weakening at high temperatures, per Azuma's model (Eqs. (8), (9); Fig. 3(g)). At low temperatures on the other hand, we intuitively expect CPO development to produce strain hardening, since c-axes progressively rotate towards hard orientations—i.e., *c*-axes inclined <20° from the compression axis (Fig. 5(e))—corresponding to $S \leq 0.3$ (Fig. 1(b)). However, our data show that even at -30 °C, where *c*-axes are rotating into hard slip orientations, the number of *c*-axes in high-S (easy slip) orientations remains significant (Figs. 5(e), 5(f)). Consequently, the bulk reduced Schmid factor, S_{bulk}, still increases with strain (Table 3(c)), and thus leads to strain weakening in Azuma's flow law (Eqs. (8), (9); Figs. 3(k, o)). The observation of many grains with *c*-axes in high-S orientations at both high and low temperatures can be explained by the rate of strain-induced GBM (which favours the growth of grains in easy slip, high-S orientations) being similar across the range of temperatures explored here (as examined by Fan et al., 2021a). GBM rates are similar among low and high temperature conditions because GBM is controlled by both grain boundary mobility and the driving force for boundary migration (Humphreys et al., 2017)—grain boundary mobility decreases with decreasing temperature (Azuma et al., 2012), whereas the GBM driving force depends on the stress magnitude (which increases with decreasing temperature, if strain rate remains unchanged—see Fig 2; Fan et al., 2021a).

4.2.3 Strain weakening mechanisms across a broader range of conditions

In the models presented here, grain size evolution (reduction) does not produce strain weakening, while CPO evolution is able to account for all of the observed weakening. Thus, we suggest that CPO development is entirely responsible for strain weakening across the range of conditions explored here (T = -4 to -30°C; strain rate ≈ 10^{-5} s^{-1}; stress ≈ 1–10 MPa). To quantify the relative contributions of CPO and grain size to strain weakening across a wider range of strain rate/stress, we compare this study with published ice uniaxial compression experiments that provide mechanical data as well as the CPO and/or grain size data (Jacka & Maccagnan, 1984; Qi et al., 2017; Vaughan et al., 2017). The EBSD data from Vaughan et al. (2017) and Qi et al. (2017) were re-processed following the same procedure used in this study (Sects. 2.2, 2.4) to acquire median grain size and bulk reduced Schmid factor, S_{bulk} measurements. Jacka & Maccagnan (1984) provide mean grain size and *c*-axis point orientation data—the *c*-axis point data were digitized using an automated algorithm in MATLAB, from which S_{bulk} measurements were calculated. For Jacka & Maccagnan (1984) and Vaughan et al. (2017), which include experiments performed to various finite shortening strains, the modelled strain rates or stresses were normalised relative to their values at the minimum strain rate or peak stress, respectively (as described above in Sect. 2.5). Qi et al. (2017), who deformed ice samples under different strain rates, only provide microstructural data at ~20% strain. Based on our experiments, the grain size at peak stress is hard to predict due to a significant grain size reduction even at low strains (Figs. 4(b)−6(b)). However, the CPO is generally still close to random at the peak stress (Figs. 4(d)−6(d)). Therefore, for the data from Qi et al. (2017), we applied only Azuma's flow law to model the mechanical effects of CPO development. The modelled stress at each finite strain was normalised relative to the peak stress estimated for a random CPO (S_{bulk} = 0.25).

For constant load/stress experiments (-4 °C series in this study; data from Jacka & Maccagnan, 1984), we calculate the ratio between the normalised measured strain rate, $\bar{\dot{\varepsilon}}_{measure}$ (Eq. (13)) and the normalised modelled strain rate, $\bar{\dot{\varepsilon}}_{model}$ (Eq. (14)) at each finite strain (Fig. 8(a)). For experiments with constant displacement rate (-10, -30 °C series in this study; data from Qi et al., 2017 and Vaughan et al., 2017), we calculate the ratio between the normalised measured stress drop, $\Delta\bar{\sigma}_{measure}$ (Eq. (16)) and the normalised modelled stress drop, $\Delta\bar{\sigma}_{model}$ (Eq. (18)) (Fig. 8(b)). Full details of these data are provided in Sect. S3 of the supplement. Figure 8 shows that the measured strain rate enhancement (for constant load/stress experiments) and stress drops (for constant displacement rate experiments) are generally close to the modelled results using Azuma's flow law, i.e., $\frac{\bar{\dot{\varepsilon}}_{measure}}{\bar{\dot{\varepsilon}}_{model(Azuma)}} \approx 1$; $\frac{\Delta\bar{\sigma}_{measure}}{\Delta\bar{\sigma}_{model(Azuma)}} \approx 1$ (purple symbols, Fig. 8). On the other hand, the Dislocation+GBS model generally underestimates the measured strain weakening, i.e., $\frac{\bar{\dot{\varepsilon}}_{measure}}{\bar{\dot{\varepsilon}}_{model(Disl.+GBS)}} > 2$; $\frac{\Delta\bar{\sigma}_{measure}}{\Delta\bar{\sigma}_{model(Disl.+GBS)}} \gg 5$ (red symbols, Fig. 8). In some cases, the Dislocation+GBS model even predicts strain hardening, i.e., $\frac{\Delta\bar{\sigma}_{measure}}{\Delta\bar{\sigma}_{model(Disl.+GBS)}} < 0$ (red symbols, Fig. 8(b)), which is at odds with the experimental observations of strain weakening. Thus, even across a broader range of strain rates than those explored in our deformation experiments, CPO development remains the dominant contributor to strain weakening. Weakening due to grain size reduction remains negligible.

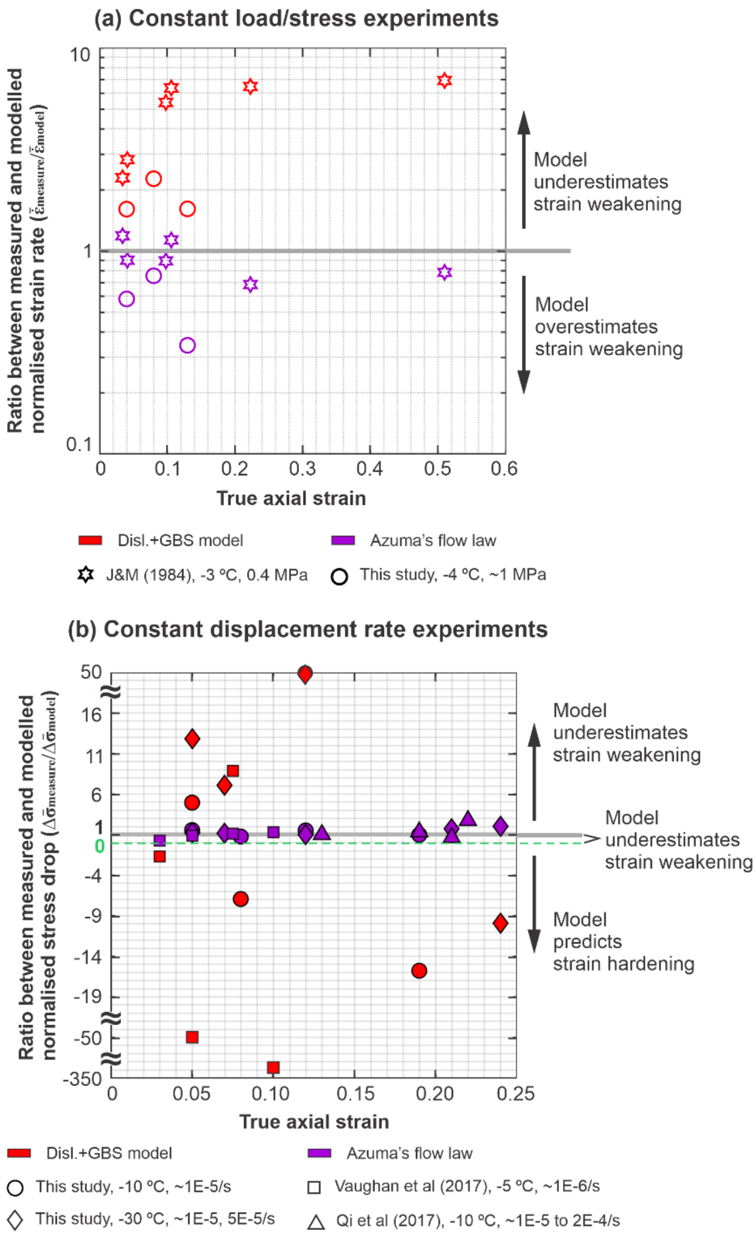

Figure 8. Modelling the relative contribution of CPO development and grain size change to the strain weakening using data from this study and published literature (Jacka & Maccagnan, 1984; Qi et al., 2017; Vaughan et al., 2017). Results using the Dislocation+GBS model (Sect. 2.3.2), which considers the grain size effects, are coloured red; results using the Azuma's flow law (Sect. 2.3.3), which considers the CPO development, are coloured purple. **(a)** For constant load experiments, at each finite strain, the ratio between measured normalised strain rate, $\bar{\dot{\varepsilon}}_{measure}$ (Eq. (13)), and modelled normalised strain rate, $\bar{\dot{\varepsilon}}_{model}$ (Eq. (14)), was calculated (Sect. 4.2.3). **(b)** For constant displacement rate experiments, at each finite strain, the ratio between measured normalised stress drop, $\Delta\bar{\sigma}_{measure}$ (Eq. (16)), and modelled normalised stress drop, $\Delta\bar{\sigma}_{model}$ (Eq. (14)), was calculated (Sect. 4.2.3).

4.3 Implications for natural ice and rock deformation

Even though all the mechanical models predict ice strengths that generally match the magnitudes of measured ice strength, only Azuma's flow law matches the observed patterns of strain weakening (Fig.2). This observation suggests that strain weakening in ice can be estimated on the basis of *c*-axis orientations alone, without regard for grain size evolution, at least under the relatively high stress, high temperature conditions explored here. Therefore, acquiring ice sheet scale measurements of *c*-axis orientation would be valuable for better constraining terrestrial ice flow mechanics and rates of ice mass discharge. Terrestrial ice c-axis data are usually provided by microstructural analyses of ice cores (e.g., Azuma et al., 1999; Weikusat et al., 2017). However, recent developments in cryo-seismology may enable a cost-effective way to estimate ice c-axes across a wide region (on the order of at least several square kilometres) via inversion of seismic anisotropy data (Smith et al., 2017).

Ice is an important analogue for minerals with strong viscous anisotropy, such as quartz and olivine (Wilson et al., 2014). Moreover, rock deformation experiments at homologous temperatures much higher than 0.7 (> 1500 K) remain challenging for many major rock-forming minerals, which has limited our understanding of high-temperature mineral microstructures and their implications for mechanical behaviour. Therefore, our study on ice samples deformed at very high homologous temperatures ($T_h \geq 0.9$) should provide valuable information on the high-temperature deformation of other viscously anisotropic minerals. For example, our experimental data suggest that at $T_h \geq 0.9$, strain weakening is dominated by CPO development, whilst the contribution of grain size reduction is generally negligible. However, at $T_h \approx 0.7$, it has been found that strain weakening in olivine is dominated by grain size reduction, with only ~30% of strain weakening arising from CPO development (Hansen et al., 2012). Together, these data indicate that strain weakening can result from both grain size reduction and CPO development; however, the relative contributions of these two processes may vary systematically across different thermomechanical conditions. Grain size reduction may dominate strain weakening at low temperatures (Hansen et al., 2012), whereas CPO development may govern strain weakening at high temperatures (this study). Constraining the processes that produce strain weakening is not just important for ice, as strain weakening is necessary for the development of localised lithospheric shear zones (White et al., 1980). Consequently, CPO development might play a central role—along with other processes such as melt band formation under partial melt conditions (King et al., 2009; Kohlstedt & Holtzman, 2009) and/or the formation of compositional layering in polymineralic rocks (Bons & Cox, 1994; Cross et al., 2020)—in shear zone nucleation and evolution at very high, near-solidus temperatures.

5 Conclusions

1. Strain weakening of initially isotropic polycrystalline ice occurs after strains of 1-3% at temperatures between -4 and -30 °C ($T_h \geq 0.9$). Grain size reduction and CPO development are observed during strain weakening.

2. Stress-grain size data from this study and published studies, combined with a composite ice flow law (Goldsby & Kohlstedt, 1997, 2001), suggest that both GBS and dislocation creep contribute to sample straining under our experimental conditions. However, the composite flow law, which includes grain size sensitivity related to grain boundary sliding, predicts a near-constant sample strength with increasing strain, in contradiction to the observed strain weakening. This result suggests that grain size reduction has little effect on strain weakening under our high homologous temperature experimental conditions.

3. Meanwhile, c-axis orientation statistics were incorporated into a flow law that solely considers the effect of CPO on bulk ice strength. The CPO-only model is able to closely

replicate the observed strain weakening, suggesting that CPO development is responsible for strain weakening at high homologous temperatures, at least for materials with strong viscous anisotropy like ice and, we suggest, possibly olivine and quartz.

4. Previous studies have found that grain size reduction plays a dominant role in strain weakening at lower homologous temperatures (Hansen et al., 2012). Our data suggest that CPO development is the more effective strain weakening mechanism at higher homologous temperatures. Together, these studies suggest that strain weakening may result from both grain size reduction and CPO development, the relative contributions of which may vary as a function of temperature, grain size, stress, and strain rate.

Appendix A. Estimate the impact of elastic deformation on plastic strain measurement for constant load experiments

For a deformed material, the measured strain using the initial and final sample dimension (e.g., Eq. (1)) comprises both elastic strain and plastic strain (Hill et al., 1947). The elastic strain, $\varepsilon_{elastic}$, is the strain that is fully recoverable after the removal of load, and it is the ratio between the applied differential stress, σ, and the Young's modulus, E:

$$\varepsilon_{elastic} = \frac{\sigma}{E} \qquad (A.1)$$

During the deformation of metal and rocks, where the applied stress is usually very high, the elastic strain should be considered in order to deduce the correct plastic strain (Hansen et al., 2012; Hill et al., 1947).

Under the setting of constant load experiments reported in this study, the assembly of walnut wood piston (Young's modulus, E_{wood}, of ~11 GPa at ~10% moisture content, Bachtiar et al., 2017) and ice (Young's modulus, E_{ice}, ~9.3 GPa, Gammon et al., 1983) was subject to an initial uniaxial stress of ~1 MPa (Sect. 2.1.2). Therefore, based on Eq. (A.1), the elastic strain of walnut wood and ice is 9.1×10^{-5} and 1.0×10^{-4}, respectively, both of which are at least two orders of magnitudes lower than the lowest strain of 0.01 achieved in the experiments. Therefore, we suggest the elastic strain of walnut wood piston and ice sample is generally insignificant, and they are negligible compared with the plastic strain of ice sample.

Appendix B. Estimate the volume fraction of different grain size classes

We estimate volume fraction for different grain size classes using the Scheil-Schwartz-Saltikov method (shortened as Saltikov method, sometimes spelled as "Saltykov method": Saltikov, 1967; Scheil, 1931; Schwartz, 1934) by assuming the grains are spherical. Numerical modelling work from Sahagian and Proussevitch (Sahagian & Proussevitch, 1998) shows that statistically, grain shape in 3-D has little effect on the grain size distributions captured by 2-D cross-sections. The Python-based GrainSizeTools toolbox (Lopez-Sanchez & Llana-Fúnez, 2016) was applied to estimate 3-D grain volume fraction from the data of grain number frequency as a function of grain size. The Saltikov method has been proven accurate in estimating the volume percentage with ±5% uncertainty for given grain size classes that correspond to the grain size class bin width of 8–16 μm (Lopez-Sanchez & Llana-Fúnez, 2016). In this study, we choose grain size class width of 10 μm as a compromise of minimising the error of individual bins in the distribution (i.e., having enough data in each class width) and grain size sensitivity in the model (i.e., having enough number of grain size classes).

Appendix C. Deformation boundary condition models

Grain size distribution has been used in grain size sensitive flow laws to quantify the control of grain size on the mechanical behaviour of deformed rock and ice (Freeman & Ferguson, 1986; Ter Heege et al., 2004; Kuiper, De Bresser, et al., 2020; Kuiper, Weikusat, et al., 2020; Rutter & Brodie, 1988). The incorporation of grain size distributions into the flow laws is based on the recognition that large and small grains may behave differently during the deformation, since the strain rates related to grain size sensitive (GSS) mechanisms, such as GBS and diffusion creep, will be faster in small grains (Ghosh & Raj, 1981; D.L. Goldsby & Kohlstedt, 1997; Rishi Raj & Ghosh, 1981). Freeman and Ferguson (1986) and Ter Heege et al. (2004) applied the following two bounding end-member deformation boundary condition models.

(1) Homogeneous stress model, with local strain rate varying from grain to grain.

(2) Homogeneous strain rate model, with local stress varying from grain to grain.

We consider an ice sample comprising i classes of grain sizes of d_A, d_B, d_C, …, d_i occupying volume fractions of v_A, v_B, v_C, …, v_i, respectively. For the homogeneous stress model (Fig. C.1(a)), we assume the stress for each grain size class equal to the bulk stress:

$$\sigma_{total} = \sigma_A = \sigma_B = \sigma_C = \cdots = \sigma_i. \tag{C.1}$$

Grain size classes have corresponding strain rates of $\dot{\varepsilon}_A$, $\dot{\varepsilon}_B$, $\dot{\varepsilon}_C$, …, $\dot{\varepsilon}_i$ (Fig. C.1(a)). The strain rate, $\dot{\varepsilon}_i$, in grain size class i is calculated using the Dislocation+GBS model (Eq. (6)). The modelled bulk strain rate, i.e., sum of volume weighted strain rates in all grain size classes, can be expressed as (Fig. C.1(a)):

$$\dot{\varepsilon}_{total} = v_A\dot{\varepsilon}_A + v_B\dot{\varepsilon}_B + v_C\dot{\varepsilon}_C + \cdots + v_i\dot{\varepsilon}_i. \tag{C.2}$$

For homogeneous strain rate model (Fig. C.1(b)), we assume the strain rate for each grain size class equals to the bulk strain rate:

$$\dot{\varepsilon}_{total} = \dot{\varepsilon}_A = \dot{\varepsilon}_B = \dot{\varepsilon}_C = \cdots = \dot{\varepsilon}_i. \tag{C.3}$$

The stress σ_i for grain size class i corresponding to the Dislocation+GBS model can be calculated by solving Eq. (6) via iteration. The modelled bulk stress, i.e., sum of volume weighted stresses in all grain size classes can be expressed as (Fig. C.1(b)):

$$\sigma_{total} = v_A\sigma_A + v_B\sigma_B + v_C\sigma_C + \cdots + v_i\sigma_i. \tag{C.4}$$

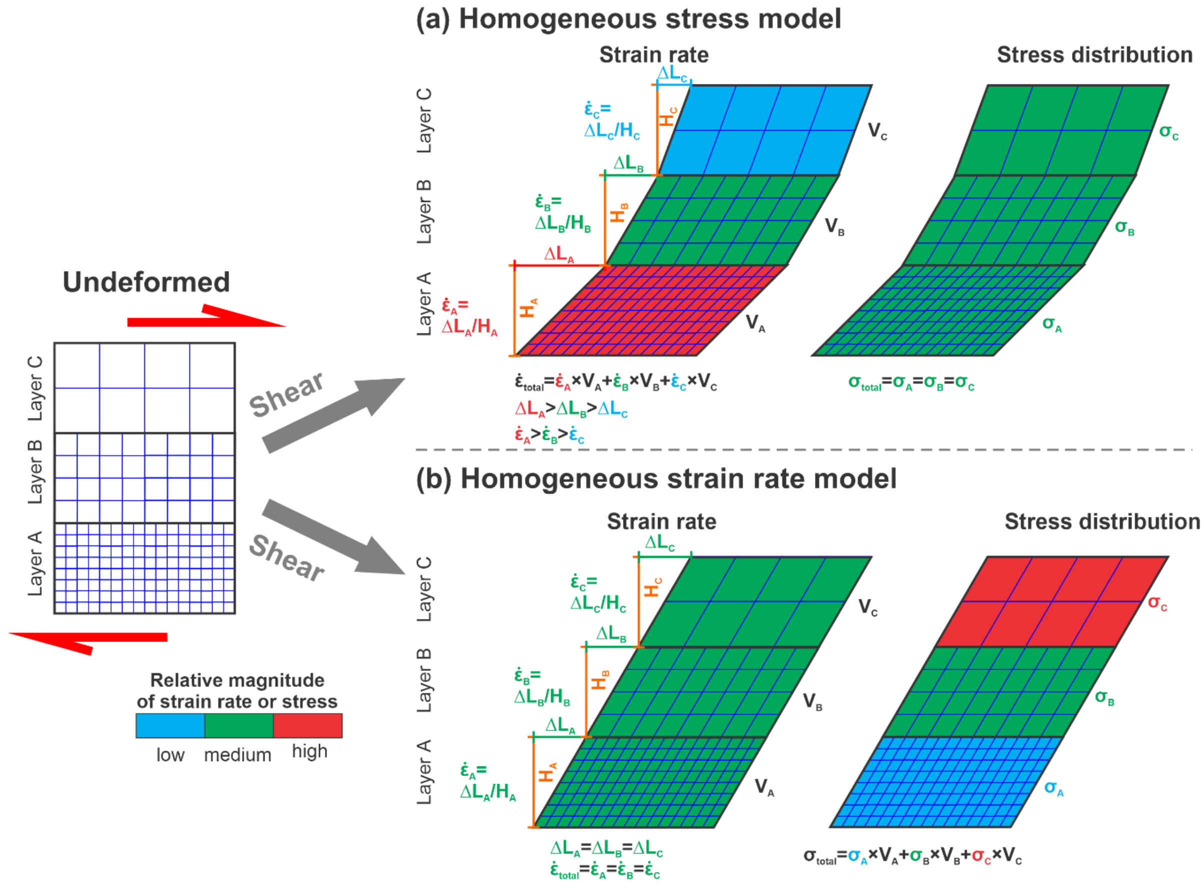

Figure C.1. Schematic drawing that illustrates principles of the two end-member deformation boundary condition models (Sect. 2.4.1; Appendix C) of **(a)** homogeneous stress with local strain rate varying from grain to grain, and **(b)** homogeneous strain rate with local stress varying from grain to grain. Note that, for the sake of simplicity and clarity of demonstration, each grain is presented with a quadrangle, and grains with the same sizes are grouped. Undeformed sample is composed by three layers of grains; each layer contains grains with the same sizes; grain size decreases from layer C to layer A. After deformation, each grain is coloured by the relative magnitude of strain rate or stress based on homogeneous stress model (**(a)**) and homogeneous strain rate model (**(b)**). For each layer, the corresponding strain rate, volume frequency and stress are marked next to it.

Appendix D. Calculate the density of *c*-axes between given co-latitude intervals

Figure D.1 is a 3-D illustration of an interval between two co-latitudes of θ_1 and θ_2 that contain a certain number frequency, f, of *c*-axes measurements. Therefore, number frequency density (Φ), i.e., number frequency per unit area, can be calculated from the ratio between number frequency, f, and the area of the co-latitude interval in 3-D, A:

$$\Phi = \frac{f}{A} \qquad (D.1)$$

The area of the co-latitude interval in 3-D, A, is the difference between the area of two spherical caps with the height of h_1 and h_2 (Fig. D.1):

$$A = A_{cap1} - A_{cap2} = 2\pi R(h_1 - h_2) \qquad (D.2)$$

Figure D.1 shows h_1 and h_2 are function of co-latitudes of θ_1 and θ_2, respectively:

$$h_1 = R(1 - cos\theta_1)$$
$$h_2 = R(1 - cos\theta_2) \qquad (D.3)$$

By combining Eqs. (D.2) and (D.3), the Eq. (D.2) can be converted to:

$$A = 2\pi R^2(cos\theta_2 - cos\theta_1) \qquad (D.4)$$

Equation (D.4) shows the area of the co-latitude interval in 3-D, A, has a positive correlation with $cos\theta_2 - cos\theta_1$, i.e., $A \propto (cos\theta_2 - cos\theta_1)$. Moreover, the number frequency density, Φ, is a function of A (Eq. (D.1)). Therefore, in this study, we calculate the number frequency density, Φ, at a given co-latitude interval using:

$$\Phi = \frac{f}{cos\theta_2 - cos\theta_1} \qquad (D.5)$$

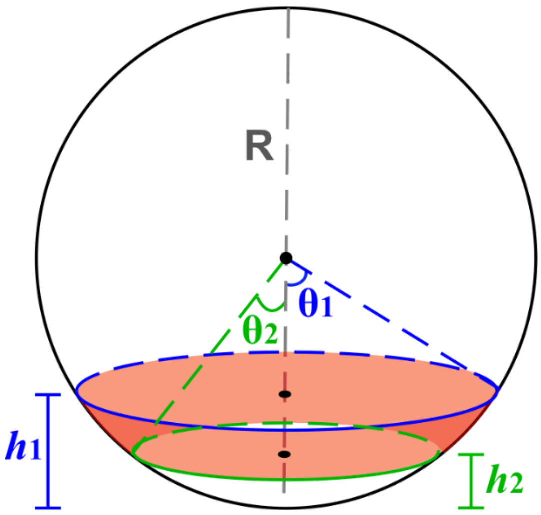

Figure D.1. A 3-D illustration of an interval between two co-latitudes of $\boldsymbol{\theta_1}$ and $\boldsymbol{\theta_2}$ that contain a certain number frequency of *c*-axes measurements.

Appendix E. Deformation mechanism maps

Goldsby (2006) and Durham et al. (2010) used a deformation mechanism map to illustrate the relevance of dislocation creep and GBS-limited creep in experimentally and naturally deformed ice. Deformation mechanism maps were introduced to summarise information about the range of dominance of distinct deformation mechanisms in a polycrystalline solid (Ashby, 1972; Frost & Ashby, 1982). Deformation mechanism maps display the relationship between the three macroscopic variables: stress (y-axis), grain size (x-axis) and strain rate (contours with dashed lines) at different temperatures (Fig. 7). The dislocation creep regime and GBS-limited creep regime are separated by a boundary displayed as a heavy black solid line, along which both mechanisms have an equal contribution to the total strain rate (Fig. 7). At each temperature, strain rate contours were calculated using corresponding flow law parameters (Table 2) for dislocation creep (Eq. (4)) and GBS-limited creep regime (Eq. (7)). The reader is reminded that the deformation mechanism boundary (displayed as a heavy black solid line) is not a separation of deformation mechanisms, the deformation mechanism regime indicates the dominant deformation mechanism. Dashed coloured lines represent the dislocation creep strain rate as ratio to the GBS-limited creep strain rate or the GBS-creep strain rate as ratio to the dislocation creep strain rate. For example, the dark-pink dashed line suggests dislocation creep strain rate is 100 times of the GBS strain rate; the red dashed line suggests GBS strain rate is 100 times of the dislocation creep strain rate (Fig.7).

We superposed stress-grain size points from experimental data from this study and published literatures (Fan et al., 2020; T.H. Jacka & Li, 1994; T.H. Jacka & Maccagnan, 1984; Vaughan et al., 2017) (Table 4, Fig.7). The stress from this study, Vaughan et al. (2017) and Fan et al. (2020) is differential axial stress. The stress from Jacka & Maccagnan (1984) and Jacka & Li (1994), were converted from reported octahedral shear stress, τ_{oct}, using:

$$\sigma = \frac{3}{\sqrt{2}}\tau_{oct} \qquad (E.1)$$

For data from this study, Vaughan et al. (2017) and Fan et al. (2020), D_{avg} is the median grain size. For data from Jacka & Maccagnan (1984), the averaged grain size, D_{avg}, is taken directly from the paper. The D_{avg} from Jacka & Maccagnan (1984) is calculated using mean linear intercept method and $D_{avg} = 1.75L/N$, where L is the length of linear transverse, N is the number of grains intercepted by the linear transverse. For data from Jacka & Li (1994), the average grain size, D_{avg}, is calculated from averaged grain area A, using:

$$D_{ave} = 2 \times \sqrt{\frac{A}{\pi}} \qquad (E.2)$$

Points projected using stress-grain size relationships correspond to estimated strain rates as constrained by the strain rate contours (thin solid black lines) in deformation mechanism maps (Fig. 7). Jacka & Li (1994) only reports a general strain range of their samples (> 0.15).

Data availability

Data can be obtained via https://doi.org/10.6084/m9.figshare.13456550 (Fan et al., 2020).

Competing interests

The authors declare that they have no conflict of interest.

Acknowledgements

We are thankful to Pat Langhorne for providing the cold-room facility at University of Otago. This work was supported by a NASA fund (grant no. NNX15AM69G) to David L. Goldsby and two Marsden Funds of the Royal Society of New Zealand (grant nos. UOO1116, UOO052) to David J. Prior. Sheng Fan was sup- ported by the University of Otago doctoral scholarship, the Antarctica New Zealand doctoral scholarship, a research grant from New Zealand Ministry of Business, Innovation and Employment through the Antarctic Science Platform (ANTA1801) (grant no. ASP-023-03), and a New Zealand Antarctic Research Institute (NZARI) Early Career Researcher Seed Grant (grant no. NZARI 2020-1-5).

References

Ashby, M. F. (1972). A first report on deformation-mechanism maps. *Acta Metallurgica*, *20*(7), 887–897. https://doi.org/10.1016/0001-6160(72)90082-X

Azuma, N., Wang, Y., Mori, K., Narita, H., Hondoh, T., Shoji, H., & Watanabe, O. (1999). Textures and fabrics in the Dome F (Antarctica) ice core. *Annals of Glaciology*, *29*, 163–168. https://doi.org/10.3189/172756499781821148

Azuma, Nobuhiko. (1994). A flow law for anisotropic ice and its application to ice sheets. *Earth and Planetary Science Letters*, *128*(3–4), 601–614. https://doi.org/10.1016/0012-821X(94)90173-2

Azuma, Nobuhiko. (1995). A flow law for anisotropic polycrystalline ice under uniaxial compressive deformation. *Cold Regions Science and Technology*, *23*(2), 137–147. https://doi.org/10.1016/0165-232X(94)00011-L

Azuma, Nobuhiko, Miyakoshi, T., Yokoyama, S., & Takata, M. (2012). Impeding effect of air bubbles on normal grain growth of ice. *Journal of Structural Geology*, *42*(C), 184–193. https://doi.org/10.1016/j.jsg.2012.05.005

Bachmann, F., Hielscher, R., & Schaeben, H. (2011). Grain detection from 2d and 3d EBSD data—Specification of the MTEX algorithm. *Ultramicroscopy*, *111*(12), 1720–1733. https://doi.org/10.1016/j.ultramic.2011.08.002

Bachtiar, E. V., Sanabria, S. J., Mittig, J. P., & Niemz, P. (2017). Moisture-dependent elastic characteristics of walnut and cherry wood by means of mechanical and ultrasonic test incorporating three different ultrasound data evaluation techniques. *Wood Science and Technology*, *51*(1), 47–67. https://doi.org/10.1007/s00226-016-0851-z

Behn, M., Goldsby, D., & Hirth, G. (2020). The role of grain-size evolution on the rheology of ice: Implications for reconciling laboratory creep data and the Glen flow law. *The Cryosphere Discussions*, (November), 1–31. https://doi.org/10.5194/tc-2020-295

Bestmann, M., & Prior, D. J. (2003). Intragranular dynamic recrystallization in naturally deformed calcite marble: Diffusion accommodated grain boundary sliding as a result of subgrain rotation recrystallization. *Journal of Structural Geology*, *25*(10), 1597–1613. https://doi.org/10.1016/S0191-8141(03)00006-3

Bons, P. D., Kleiner, T., Llorens, M. G., Prior, D. J., Sachau, T., Weikusat, I., & Jansen, D. (2018). Greenland Ice Sheet: Higher Nonlinearity of Ice Flow Significantly Reduces Estimated Basal Motion. *Geophysical Research Letters*, *45*(13), 6542–6548. https://doi.org/10.1029/2018GL078356

Bons, Paul D., & Cox, S. J. D. (1994). Analogue experiments and numerical modelling on the relation between microgeometry and flow properties of polyphase materials. *Materials Science and Engineering A*, *175*(1–2), 237–245. https://doi.org/10.1016/0921-5093(94)91063-4

Braun, J., Chéry, J., Poliakov, A., Mainprice, D., Vauchez, A., Tomassi, A., & Daignières, M. (1999). A simple parameterization of strain localization in the ductile regime due to grain size reduction: A case study for olivine. *Journal of Geophysical Research: Solid Earth*, *104*(B11), 25167–25181. https://doi.org/10.1029/1999JB900214

De Bresser, J. H. P., Ter Heege, J. H., & Spiers, C. J. (2001). Grain size reduction by dynamic recrystallization: Can it result in major rheological weakening? *International Journal of Earth Sciences*, *90*(1), 28–45. https://doi.org/10.1007/s005310000149

Budd, W.F., & Jacka, T. H. (1989). A review of ice rheology for ice sheet modelling. *Cold Regions Science and Technology*, *16*(2), 107–144. https://doi.org/10.1016/0165-232X(89)90014-1

Budd, William F., Warner, R. C., Jacka, T. H., Li, J., & Treverrow, A. (2013). Ice flow relations for stress and strain-rate components from combined shear and compression laboratory experiments. *Journal of Glaciology*, *59*(214), 374–392. https://doi.org/10.3189/2013JoG12J106

Castelnau, O., Duval, P., Lebensohn, R. A., & Canova, G. R. (1996). Viscoplastic modeling of texture development in polycrystalline ice with a self-consistent approach: Comparison with bound estimates. *Journal of Geophysical Research B: Solid Earth*, *101*(6), 13851–13868. https://doi.org/10.1029/96jb00412

Cole, D. M. (1979). Preparation of polycrystalline ice specimens for laboratory experiments. *Cold Regions Science and Technology*, *1*(2), 153–159. https://doi.org/10.1016/0165-232X(79)90007-7

Cross, A. J., & Skemer, P. (2017). Ultramylonite generation via phase mixing in high-strain experiments. *Journal of Geophysical Research: Solid Earth*, *122*(3), 1744–1759. https://doi.org/10.1002/2016JB013801

Cross, A. J., & Skemer, P. (2019). Rates of Dynamic Recrystallization in Geologic Materials. *Journal of Geophysical Research: Solid Earth*, *124*(2), 1324–1342. https://doi.org/10.1029/2018JB016201

Cross, Andrew J., Olree, E., Couvy, H., & Skemer, P. (2020). How Does Viscosity Contrast Influence Phase Mixing and Strain Localization? *Journal of Geophysical Research: Solid Earth*, *125*(8), 1–20. https://doi.org/10.1029/2020JB020323

Cuffey, K. M., & Paterson, W. S. B. (2010). *The Physics of Glaciers* (4th ed.). Butterworth-Heinemann.

Derby, B., & Ashby, M. F. F. (1987). On dynamic recrystallisation. *Scripta Metallurgica*, *21*(6), 879–884. https://doi.org/10.1016/0036-9748(87)90341-3

Döhmann, M. J. E. A., Brune, S., Nardini, L., Rybacki, E., & Dresen, G. (2019). Strain Localization and Weakening Processes in Viscously Deforming Rocks: Numerical Modeling Based on Laboratory Torsion Experiments. *Journal of Geophysical Research: Solid Earth*, *124*(1), 1120–1137. https://doi.org/10.1029/2018JB016917

Drury, M. R. (2005). Dynamic recrystallization and strain softening of olivine aggregates in the laboratory and the lithosphere. *Geological Society Special Publication*, *243*(2), 143–158. https://doi.org/10.1144/GSL.SP.2005.243.01.11

Durham, W. B., Prieto-Ballesteros, O., Goldsby, D. L., & Kargel, J. S. (2010). Rheological and thermal properties of icy materials. *Space Science Reviews*, *153*(1–4), 273–298. https://doi.org/10.1007/s11214-009-9619-1

Durham, W B, Heard, H. C., & Kirby, S. H. (1983). Experimental deformation of polycrystalline H 2 O ice at high pressure and low temperature: Preliminary results. *Journal of Geophysical Research*, *88*(S01), B377. https://doi.org/10.1029/JB088iS01p0B377

Durham, William B., Kirby, S. H., & Stern, L. A. (1992). Effects of dispersed particulates on the rheology of water ice at planetary conditions. *Journal of Geophysical Research*, *97*(E12), 20883. https://doi.org/10.1029/92je02326

Duval, P., Ashby, M. F., & Anderman, I. (1983). Rate-controlling processes in the creep of polycrystalline ice. *Journal of Physical Chemistry*, *87*(21), 4066–4074. https://doi.org/10.1021/j100244a014

Duval, Paul. (1979). Creep and recrystallization of polycrystalline ice. *Bulletin de Minéralogie*, *102*(2), 80–85. https://doi.org/10.3406/bulmi.1979.7258

Etheridge, M. A., & Wilkie, J. C. (1979). Grainsize reduction, grain boundary sliding and the flow strength of mylonites. *Tectonophysics*, *58*(1–2), 159–178. https://doi.org/10.1016/0040-1951(79)90327-5

Fan, S., Hager, T. F., Prior, D. J., Cross, A. J., Goldsby, D. L., Qi, C., et al. (2020). Temperature and strain controls on ice deformation mechanisms: insights from the microstructures of samples deformed to progressively higher strains at −10, −20 and −30 °C. *The Cryosphere*, *14*(11), 3875–3905. https://doi.org/10.5194/tc-14-3875-2020

Fan, S., Prior, D. J., Cross, A. J., Goldsby, D. L., Hager, T. F., Negrini, M., & Qi, C. (2021a). Using grain boundary irregularity to quantify dynamic recrystallization in ice. *Acta Materialia*, *209*, 116810. https://doi.org/10.1016/j.actamat.2021.116810

Fan, S., Prior, D. J., Hager, T. F., Cross, A. J., Goldsby, D. L., & Negrini, M. (2021b). Kinking facilitates grain nucleation and modifies crystallographic preferred orientations during high-stress ice deformation. *Earth and Planetary Science Letters*, *572*, 117136. https://doi.org/10.1016/j.epsl.2021.117136

Freeman, B., & Ferguson, C. C. (1986). Deformation mechanism maps and micromechanics of rocks with distributed grain sizes. *Journal of Geophysical Research: Solid Earth*, *91*(B3), 3849–3860. https://doi.org/10.1029/jb091ib03p03849

Frost, H. J., & Ashby, M. F. (1982). *Deformation mechanism maps: the plasticity and creep of metals and ceramics*. Pergamon Press. Retrieved from https://engineering.dartmouth.edu/defmech/

Gammon, P. H., Kiefte, H., Clouter, M. J., & Denner, W. W. (1983). Elastic constants of artificial and natural ice samples by Brillouin spectroscopy. *Journal of Glaciology*, *29*(103), 433–460. https://doi.org/10.1017/S0022143000030355

Gao, X. Q., & Jacka, T. H. (1987). Approach To Similar Tertiary Creep Rates for Antarctic Core Ice and Laboratory Prepared Ice. *Journal de Physique (Paris), Colloque*, *48*(3), 289–296. https://doi.org/10.1051/jphyscol:1987141

Gerbi, C., Mills, S., Clavette, R., Campbell, S., Bernsen, S., Clemens-Sewall, D., et al. (2021). Microstructures in a shear margin: Jarvis Glacier, Alaska. *Journal of Glaciology*, 1–14. https://doi.org/10.1017/jog.2021.62

Ghosh, A. K., & Raj, R. (1981). Grain size distribution effects in superplasticity. *Acta Metallurgica*, *29*(4), 607–616. https://doi.org/10.1016/0001-6160(81)90142-5

Gifkins, R. C. (1976). Grain-boundary sliding and its accommodation during creep and superplasticity. *Metallurgical Transactions A*, *7*(8), 1225–1232. https://doi.org/10.1007/BF02656607

Gillet-Chaulet, F., Gagliardini, O., Seddik, H., Nodet, M., Durand, G., Ritz, C., et al. (2012). Greenland ice sheet contribution to sea-level rise from a new-generation ice-sheet model. *Cryosphere*, *6*(6), 1561–1576. https://doi.org/10.5194/tc-6-1561-2012

Glen, J. W. (1952). Experiments on the Deformation of Ice. *Journal of Glaciology*, *2*(12), 111–114. https://doi.org/10.1017/s0022143000034067

Glen, J. W. (1953). Rate of Flow of Polycrystalline Ice. *Nature*, *172*(4381), 721–722. https://doi.org/10.1038/172721a0

Glen, J. W. (1955). The creep of polycrystalline ice. *Proceedings of the Royal Society of London. Series A. Mathematical and Physical Sciences*, *228*(1175), 519–538. https://doi.org/10.1098/rspa.1955.0066

Goldsby, D. L., & Kohlstedt, D. L. (2001). Superplastic deformation of ice: Experimental observations. *Journal of Geophysical Research: Solid Earth*, *106*(B6), 11017–11030. https://doi.org/10.1029/2000jb900336

Goldsby, D.L., & Kohlstedt, D. L. (1997). Grain boundary sliding in fine-grained Ice I. *Scripta Materialia*, *37*(9), 1399–1406. https://doi.org/10.1016/S1359-6462(97)00246-7

Goldsby, David L. (2006). Superplastic Flow of Ice Relevant to Glacier and Ice-Sheet Mechanics. In *Glacier Science and Environmental Change* (pp. 308–314). Malden, MA, USA: Blackwell Publishing. https://doi.org/10.1002/9780470750636.ch60

Gow, A. J., & Williamson, T. (1976). Rheological implications of the internal structure and crystal fabrics of the West Antarctic ice sheet as revealed by deep core drilling at Byrd Station. *Geological Society of America Bulletin*, *87*(12), 1665. https://doi.org/10.1130/0016-7606(1976)87<1665:RIOTIS>2.0.CO;2

Graversen, R. G., Drijfhout, S., Hazeleger, W., van de Wal, R., Bintanja, R., & Helsen, M. (2011). Greenland's contribution to global sea-level rise by the end of the 21st century. *Climate Dynamics*, *37*(7–8), 1427–1442. https://doi.org/10.1007/s00382-010-0918-8

Hansen, L. N., Zimmerman, M. E., & Kohlstedt, D. L. (2012). The influence of microstructure on deformation of olivine in the grain-boundary sliding regime. *Journal of Geophysical Research*, *117*(B9), 117–149.

Heard, H. C., Durham, W. B., Boro, C. O., & Kirby, S. H. (1990). A triaxial deformation apparatus for service at 77 ≤ T ≤ 273 K. In *The Brittle-Ductile Transition in Rocks* (Vol. 56, pp. 225–228). https://doi.org/10.1029/GM056p0225

Ter Heege, J. H., De Bresser, J. H. P., & Spiers, C. J. (2004). Composite flow laws for crystalline materials with log-normally distributed grain size: Theory and application to olivine. *Journal of Structural Geology*, *26*(9), 1693–1705. https://doi.org/10.1016/j.jsg.2004.01.008

Hill, R., Lee, E. H., & Tupper, S. J. (1947). The theory of combined plastic and elastic deformation with particular reference to a thick tube under internal pressure. *Proceedings of the Royal Society of London. Series A. Mathematical and Physical Sciences*, *191*(1026), 278–303. https://doi.org/10.1098/rspa.1947.0116

Hirth, G., & Kohlstedt, D. L. (1995). Experimental constraints on the dynamics of the partially molten upper mantle 2. Deformation in the dislocation creep regime. *Journal of Geophysical Research*, *100*(B8), 1981–2001. https://doi.org/10.1029/95jb01292

Holtzman, B. K., Chrysochoos, A., & Daridon, L. (2018). A Thermomechanical Framework for Analysis of Microstructural Evolution: Application to Olivine Rocks at High Temperature. *Journal of Geophysical Research: Solid Earth*, *123*(10), 8474–8507. https://doi.org/10.1029/2018JB015613

Hruby, K., Gerbi, C., Koons, P., Campbell, S., Martín, C., & Hawley, R. (2020). The impact of temperature and crystal orientation fabric on the dynamics of mountain glaciers and ice streams. *Journal of Glaciology*, *66*(259), 755–765.

https://doi.org/10.1017/jog.2020.44

Humphreys, F. J., Hatherly, M., & Rollett, A. (2017). *Recrystallization and Related Annealing Phenomena* (Third). Elsevier Ltd. Retrieved from https://www.sciencedirect.com/book/9780080982359/recrystallization-and-related-annealing-phenomena

Jacka, T.H., & Li, J. (1994). The steady-state crystal size of deforming ice. *Annals of Glaciology*, *20*, 13–18. https://doi.org/10.1017/S0260305500016165

Jacka, T.H., & Maccagnan, M. (1984). Ice crystallographic and strain rate changes with strain in compression and extension. *Cold Regions Science and Technology*, *8*(3), 269–286. https://doi.org/10.1016/0165-232X(84)90058-2

Jacka, Tim H, & Li, J. (2000). Flow rates and crystal orientation fabrics in compression of polycrystalline ice at low temperatures and stresses. In *International Symposium on Physics of Ice Core Records* (pp. 83–102). Hokkaido University Press. Retrieved from http://hdl.handle.net/2115/32463

Jansen, D., Llorens, M. G., Westhoff, J., Steinbach, F., Kipfstuhl, S., Bons, P. D., et al. (2016). Small-scale disturbances in the stratigraphy of the NEEM ice core: Observations and numerical model simulations. *Cryosphere*, *10*(1), 359–370. https://doi.org/10.5194/tc-10-359-2016

Journaux, B., Kalousová, K., Sotin, C., Tobie, G., Vance, S., Saur, J., et al. (2020). Large Ocean Worlds with High-Pressure Ices. *Space Science Reviews*, *216*(1). https://doi.org/10.1007/s11214-019-0633-7

Kamb, B. (2001). Basal Zone of the West Antarctic Ice Streams and its Role in Lubrication of Their Rapid Motion. In R. B. Alley & R. A. Bindschadle (Eds.), *Antarctic Research Series* (Vol. 77, pp. 157–199). Washington, DC: American Geophysical Union. https://doi.org/10.1029/AR077p0157

Kilian, R., Heilbronner, R., & Stünitz, H. (2011). Quartz grain size reduction in a granitoid rock and the transition from dislocation to diffusion creep. *Journal of Structural Geology*, *33*(8), 1265–1284.

King, D. S. H., Zimmerman, M. E., & Kohlstedt, D. L. (2009). Stress-driven melt segregation in partially molten olivine-rich rocks deformed in torsion. *Journal of Petrology*, *51*(1–2), 21–42. https://doi.org/10.1093/petrology/egp062

Kohlstedt, D. L., & Holtzman, B. K. (2009). Shearing melt out of the earth: An experimentalist's perspective on the influence of deformation on melt extraction. *Annual Review of Earth and Planetary Sciences*, *37*, 561–593. https://doi.org/10.1146/annurev.earth.031208.100104

Kuiper, E. J. N., Weikusat, I., De Bresser, J. H. P., Jansen, D., Pennock, G. M., & Drury, M. R. (2020a). Using a composite flow law to model deformation in the NEEM deep ice core, Greenland-Part 1: The role of grain size and grain size distribution on deformation of the upper 2207m. *Cryosphere*, *14*(7), 2429–2448. https://doi.org/10.5194/tc-14-2429-2020

Kuiper, E. J. N., De Bresser, J. H. P., Drury, M. R., Eichler, J., Pennock, G. M., & Weikusat, I. (2020b). Using a composite flow law to model deformation in the NEEM deep ice core, Greenland-Part 2: The role of grain size and premelting on ice deformation at high homologous temperature. *Cryosphere*, *14*(7), 2449–2467. https://doi.org/10.5194/tc-14-2449-2020

Lile, R. C. (1978). The Effect of Anisotropy on the Creep of Polycrystalline Ice. *Journal of Glaciology*, *21*(85), 475–483. https://doi.org/10.3189/S0022143000033621

Little, T. A., Prior, D. J., Toy, V. G., & Lindroos, Z. R. (2015). The link between strength of lattice preferred orientation, second phase content and grain boundary migration: A case study from the Alpine Fault zone, New Zealand. *Journal of Structural Geology*, *81*(C), 59–77.

Llorens, M. G., Griera, A., Bons, P. D., Roessiger, J., Lebensohn, R., Evans, L., & Weikusat, I. (2016). Dynamic recrystallisation of ice aggregates during co-axial viscoplastic deformation: A numerical approach. *Journal of Glaciology*, *62*(232), 359–377. https://doi.org/10.1017/jog.2016.28

Lopez-Sanchez, M. A. (2020). Which average, how many grains, and how to estimate robust confidence intervals in unimodal grain size populations. *Journal of Structural Geology*, *135*, 104042. https://doi.org/10.1016/j.jsg.2020.104042

Lopez-Sanchez, M. A., & Llana-Fúnez, S. (2016). An extension of the Saltykov method to quantify 3D grain size distributions in mylonites. *Journal of Structural Geology*, *93*, 149–161. https://doi.org/10.1016/j.jsg.2016.10.008

McQueen, H. J., & Jonas, J. J. (1975). Recovery and Recrystallization during High Temperature Deformation. In *Plast Deform of Mater* (Vol. 6, pp. 393–493). ACADEMIC PRESS, INC. https://doi.org/10.1016/B978-0-12-341806-7.50014-3

Mellor, M., & Cole, D. M. (1982). Deformation and failure of ice under constant stress or constant strain-rate. *Cold Regions Science and Technology*, *5*(3), 201–219. https://doi.org/10.1016/0165-232X(82)90015-5

Morland, L. W., & Staroszczyk, R. (2009). Ice viscosity enhancement in simple shear and uni-axial compression due to crystal rotation. *International Journal of Engineering Science*, *47*(11–12), 1297–1304. https://doi.org/10.1016/j.ijengsci.2008.09.011

Piazolo, S., Wilson, C. J. L., Luzin, V., Brouzet, C., & Peternell, M. (2013). Dynamics of ice mass deformation: Linking processes to rheology, texture, and microstructure. *Geochemistry, Geophysics, Geosystems*, *14*(10), 4185–4194. https://doi.org/10.1002/ggge.20246

Placidi, L., Greve, R., Seddik, H., & Faria, Se. H. (2010). Continuum-mechanical, Anisotropic Flow model for polar ice masses, based on an anisotropic Flow Enhancement factor. *Continuum Mechanics and Thermodynamics*, *22*(3), 221–237.

Poirier, J. P. (1980). Shear localization and shear instability in materials in the ductile field. *Journal of Structural Geology*, *2*(1–2), 135–142. https://doi.org/10.1016/0191-8141(80)90043-7

Prior, D. J., Lilly, K., Seidemann, M., Vaughan, M., Becroft, L., Easingwood, R., et al. (2015). Making EBSD on water ice routine. *Journal of Microscopy*, *259*(3), 237–256. https://doi.org/10.1111/jmi.12258

Qi, C., Goldsby, D. L., & Prior, D. J. (2017). The down-stress transition from cluster to cone fabrics in experimentally deformed ice. *Earth and Planetary Science Letters*, *471*, 136–147. https://doi.org/10.1016/j.epsl.2017.05.008

Raj, R., & Ashby, M. F. (1971). On grain boundary sliding and diffusional creep. *Metallurgical Transactions*, *2*(4), 1113–1127. https://doi.org/10.1007/BF02664244

Raj, Rishi, & Ghosh, A. K. (1981). Micromechanical modelling of creep using distributed parameters. *Acta Metallurgica*, *29*(2), 283–292. https://doi.org/10.1016/0001-6160(81)90155-3

Ranalli, G. (1984). Grain size distribution and flow stress in tectonites. *Journal of Structural Geology*, *6*(4), 443–447. https://doi.org/10.1016/0191-8141(84)90046-4

Rathmann, N. M., & Lilien, D. A. (2021). Inferred basal friction and mass flux affected by crystal-orientation fabrics. *Journal of Glaciology*. https://doi.org/10.1017/jog.2021.88

Rutter, E. H. (1999). On the relationship between the formation of shear zones and the form of the flow law for rocks undergoing dynamic recrystallization. *Tectonophysics*, *303*(1–4), 147–158. https://doi.org/10.1016/S0040-1951(98)00261-3

Rutter, E. H., & Brodie, K. H. (1988). The role of tectonic grain size reduction in the rheological stratification of the lithosphere. *Geologische Rundschau*, *77*(1), 295–307. https://doi.org/10.1007/BF01848691

Sahagian, D. L., & Proussevitch, A. A. (1998). 3D particle size distributions from 2D observations: stereology for natural applications. *Journal of Volcanology and Geothermal Research*, *84*(3–4), 173–196. https://doi.org/10.1016/S0377-0273(98)00043-2

Saltikov, S. A. (1967). The Determination of the Size Distribution of Particles in an Opaque Material from a Measurement of the Size Distribution of Their Sections. In H. Elias (Ed.), *Stereology* (Vol. 53, pp. 163–173). Berlin, Heidelberg: Springer Berlin Heidelberg. https://doi.org/10.1007/978-3-642-88260-9_31

Scheil, E. (1931). Die Berechnung der Anzahl und Größenverteilung kugelförmiger Kristalle in undurchsichtigen Körpern mit Hilfe der durch einen ebenen Schnitt erhaltenen Schnittkreise. *Zeitschrift Für Anorganische Und Allgemeine Chemie*, *201*(1), 259–264. https://doi.org/10.1002/zaac.19312010123

Schmid, S. M., Boland, J. N., & Paterson, M. S. (1977). Superplastic flow in finegrained limestone. *Tectonophysics*, *43*(3–4), 257–291. https://doi.org/10.1016/0040-1951(77)90120-2

Schwartz, H. A. (1934). The metallographic determination of the size distribution of temper carbon nodules. *Metals Alloys*, *5*, 139.

Sellars, C. M. (1978). Recrystallization of metals during hot deformation. *Philosophical Transactions of the Royal Society of London. Series A, Mathematical and Physical Sciences*, *288*(1350), 147–158. https://doi.org/10.1098/rsta.1978.0010

Shoji, H., & Langway, C. C. (1988). Flow-Law Parameters of the Dye 3, Greenland, Deep Ice Core. *Annals of Glaciology*, *10*, 146–150. https://doi.org/10.3189/s026030550000433x

Shoji, Hitoshi, & Langway, C. C. (1984). Flow Behavior of Basal Ice as Related to Modeling Considerations. *Annals of Glaciology*, *5*(c), 141–148. https://doi.org/10.3189/1984AoG5-1-141-148

Skemer, P., Warren, J. M., Kelemen, P. B., & Hirth, G. (2009). Microstructural and rheological evolution of a mantle shear zone. *Journal of Petrology*, *51*(1–2), 43–53. https://doi.org/10.1093/petrology/egp057

Smith, E. C., Baird, A. F., Kendall, J. M., Martín, C., White, R. S., Brisbourne, A. M., & Smith, A. M. (2017). Ice fabric in an Antarctic ice stream interpreted from seismic anisotropy. *Geophysical Research Letters*, *44*(8), 3710–3718.

https://doi.org/10.1002/2016GL072093

Soleymani, H., Kidder, S., Hirth, G., & Garapić, G. (2020). The effect of cooling during deformation on recrystallized grain-size piezometry. *Geology*, *48*(6), 531–535. https://doi.org/10.1130/G46972.1

Treverrow, A., Budd, W. F., Jacka, T. H., & Warner, R. C. (2012). The tertiary creep of polycrystalline ice: Experimental evidence for stress-dependent levels of strain-rate enhancement. *Journal of Glaciology*, *58*(208), 301–314. https://doi.org/10.3189/2012JoG11J149

Vaughan, M. J., Prior, D. J., Jefferd, M., Brantut, N., Mitchell, T. M., & Seidemann, M. (2017). Insights into anisotropy development and weakening of ice from in situ P wave velocity monitoring during laboratory creep. *Journal of Geophysical Research: Solid Earth*, *122*(9), 7076–7089. https://doi.org/10.1002/2017JB013964

van der Veen, C. J., & Whillans, I. M. (1994). Development of fabric in ice. *Cold Regions Science and Technology*, *22*(2), 171–195. https://doi.org/10.1016/0165-232X(94)90027-2

Warren, J. M., & Hirth, G. (2006). Grain size sensitive deformation mechanisms in naturally deformed peridotites. *Earth and Planetary Science Letters*, *248*(1–2), 438–450. https://doi.org/10.1016/j.epsl.2006.06.006

Weertman, J. (1983). Creep Deformation of Ice. *Annual Review of Earth and Planetary Sciences*, *11*(1), 215–240. https://doi.org/10.1146/annurev.ea.11.050183.001243

Weikusat, I., Jansen, D., Binder, T., Eichler, J., Faria, S. H., Wilhelms, F., et al. (2017). Physical analysis of an Antarctic ice core-towards an integration of micro-and macrodynamics of polar ice. *Philosophical Transactions of the Royal Society A: Mathematical, Physical and Engineering Sciences*, *375*(2086). https://doi.org/10.1098/rsta.2015.0347

White, S. (1976). The Effects of Strain on the Microstructures, Fabrics, and Deformation Mechanisms in Quartzites. *Philosophical Transactions of the Royal Society A: Mathematical and Physical Sciences*, *283*(1312), 69–86. Retrieved from https://www.jstor.org/stable/74630

White, S. H., Burrows, S. E., Carreras, J., Shaw, N. D., & Humphreys, F. J. (1980). On mylonites in ductile shear zones. *Journal of Structural Geology*, *2*(1–2), 175–187. https://doi.org/10.1016/0191-8141(80)90048-6

Wilson, C. J. L., Peternell, M., Piazolo, S., & Luzin, V. (2014). Microstructure and fabric development in ice: Lessons learned from in situ experiments and implications for understanding rock evolution. *Journal of Structural Geology*, *61*, 50–77. https://doi.org/10.1016/j.jsg.2013.05.006

Table 1(a) Summary of the mechanical and grain size data for uniaxial compression experiments with constant load

Sample No.	T (°C)	Final true axial strain	Minimum true axial strain rate	Stress at minimum true axial strain rate	True axial strain at minimum true axial strain rate	Final true axial strain rate	[1]Final stress	Grain number	Grain size parameters (μm)					
		ε_f	$\dot{\varepsilon}_m$ (s^-1^)	σ_m (MPa)	ε_m	$\dot{\varepsilon}_f$ (s^-1^)	σ_f (MPa)		Peak	Mean	Median	Lower quartile	Higher quartile	Interquartile range (IQR)
Undeformed	N/A	N/A	N/A	N/A	N/A	N/A	N/A	653	600	535	545	359	730	371
OIL009	-4	0.01	N/A	N/A	N/A	1.11×10^{-6}	1.02	2880	357	542	501	340	693	353
OIL008		0.04	Not recorded	Not recorded	Not recorded	$^*1.40 \times 10^{-6}$	0.99	1716	176	536	453	258	725	467
OIL007		0.08	7.60×10^{-7}	1.01	0.02	1.78×10^{-6}	0.95	1569	164	419	411	243	707	464
OIL006		0.13	6.54×10^{-7}	1.01	0.02	1.22×10^{-6}	0.90	2309	161	561	337	222	535	313
OIL041		0.13	9.74×10^{-7}	1.01	0.02	1.58×10^{-6}	0.90	N/A						
OIL042		0.13	9.43×10^{-7}	1.01	0.02	1.67×10^{-6}	0.90							
OIL044		0.13	8.44×10^{-7}	1.01	0.02	1.48×10^{-6}	0.90							
OIL045		0.13	8.41×10^{-7}	1.01	0.02	1.57×10^{-6}	0.90							

[1] Estimated from load and change of sample cross-sectional area, assuming constant sample volume during the deformation (Eq. (3)).

[*] Estimated from an average of true axial strain rate at 4% strain from experiments with $\varepsilon_f \geq 8\%$.

Table 1(b) Summary of the mechanical and grain size data for uniaxial compression experiments with constant displacement rate

Sample No.	T (°C)	Final true axial strain	Peak stress	True axial strain rate at peak stress	True axial strain at peak stress	Final stress	True axial strain rate at final stress	Grain number	Grain size parameters (μm)					
		ε_f	σ_p (MPa)	$\dot{\varepsilon}_p$ (s^{-1})	ε_p	σ_f (MPa)	$\dot{\varepsilon}_f$ (s^{-1})		Peak	Mean	Median	Lower quartile	Higher quartile	Interquartile range (IQR)
Undeformed	N/A	N/A	N/A	N/A	N/A	N/A	N/A	1242	300	297	291	165	413	248
PIL176		0.03	1.78	1.03×10^{-5}	0.02	1.70	1.04×10^{-5}	548	29	163	126	52	256	204
PIL163		0.05	2.92	1.03×10^{-5}	0.01	2.42	1.06×10^{-5}	1282	38	126	98	57	171	114
PIL178	-10	0.08	2.54	1.11×10^{-5}	0.02	1.97	1.19×10^{-5}	894	49	140	118	72	186	114
PIL177		0.12	2.85	1.11×10^{-5}	0.03	1.90	1.21×10^{-5}	1300	39	115	92	57	154	97
PIL007		0.19	2.13	1.03×10^{-5}	0.02	1.33	1.22×10^{-5}	1523	37	106	87	51	142	91
PIL165		0.03	8.24	1.08×10^{-5}	0.03	8.15	1.09×10^{-5}	4923	32	145	103	51	225	174
PIL162		0.05	8.71	1.07×10^{-5}	0.03	7.87	1.10×10^{-5}	2098	33	105	78	47	136	89
PIL164		0.07	8.93	1.03×10^{-5}	0.03	7.31	1.07×10^{-5}	1259	31	101	64	41	112	71
PIL166	-30	0.12	7.60	1.11×10^{-5}	0.03	6.45	1.20×10^{-5}	5447	29	68	55	39	80	41
PIL268		0.21	7.82	1.10×10^{-5}	0.02	5.00	1.31×10^{-5}	6809	23	62	38	30	56	26
PIL266		0.03	11.29	5.40×10^{-5}	0.03	11.26	5.40×10^{-5}	1342	36	135	115	53	200	147
PIL243		0.24	10.63	5.40×10^{-5}	0.03	7.35	6.70×10^{-5}	9259	23	51	39	30	55	25

Table 3(a) Summary of measured and estimated strain rate for experiments with constant load at -4 °C

Sample No.	T (°C)	Initial stress (MPa)	Measured minimum strain rate (s^{-1})	Measured strain rate (s^{-1}) at maximum strain, absolute /normalised	Estimated strain rate (s^{-1}), absolute/normalised		**Dislocation+GBS model (simplified Goldsby-Kohlstedt composite flow law)**		Bulk reduced Schmid factor, S_{bulk}	Estimated strain rate (s^{-1}), absolute/normalised	
					Glen's flow law	**Durham's flow law**	Strain rate (s^{-1}) estimated from grain size distribution, absolute /normalised	Strain rate (s^{-1}) estimated from median grain size, absolute /normalised		**Azuma's flow law**	
										With upper bound of #$\boldsymbol{B}$	With lower bound of $\boldsymbol{B}$
Undeformed medium-grained	N/A	N/A	N/A	N/A	N/A	N/A	N/A	N/A	0.2449	N/A	N/A
OIL009	-4	~1	N/A	1.11×10^{-6} /1.00	1.80×10^{-6} /1.00	1.39×10^{-6} /1.00	7.63×10^{-7} /1.00	1.10×10^{-6} /1.00	0.2514	6.92×10^{-7} /1.00	7.59×10^{-8} /1.00
OIL008			Not recorded	Not recorded	1.70×10^{-6} /0.94	1.28×10^{-6} /0.92	6.37×10^{-7} /0.83	1.20×10^{-6} /1.09	0.3239	2.01×10^{-6} /2.90	2.56×10^{-7} /3.37
OIL007			7.60×10^{-7}	1.78×10^{-6} /2.34	1.49×10^{-6} /0.82	1.07×10^{-6} /0.77	6.14×10^{-7} /0.80	1.30×10^{-6} /1.19	0.3295	2.16×10^{-6} /3.12	2.78×10^{-7} /3.66
OIL006			6.54×10^{-7}	1.22×10^{-6} /1.87	1.30×10^{-6} /0.72	9.01×10^{-7} /0.65	7.50×10^{-7} /0.98	1.60×10^{-6} /1.45	0.3766	3.78×10^{-6} /5.46	5.28×10^{-7} /6.96

A pre-exponential term, which generally has a power law relationship with S_{bulk} (Eq. (10)).

Table 3(b) Summary of measured and estimated stress for experiments with constant displacement rate at -10 °C

Sample No.	T (°C)	Initial strain rate (s^{-1})	Measured peak stress (MPa)	Measured stress (MPa) at maximum strain, absolute /normalised	Estimated stress (MPa), absolute/normalised: **Glen's flow law**	**Durham's flow law**	**Dislocation+GBS model (simplified Goldsby-Kohlstedt composite flow law)**: Stress estimated (MPa) from grain size distribution, absolute /normalised	Stress (MPa) estimated from median grain size, absolute /normalised	Bulk reduced Schmid factor, S_{bulk}	Estimated stress (MPa), absolute/normalised, **Azuma's flow law**: With upper bound of ***B***	With lower bound of ***B***
Undeformed standard ice	N/A	N/A	N/A	N/A	N/A	N/A	N/A	N/A	0.2438	N/A	N/A
PIL176	-10	$\sim 1 \times 10^{-5}$	1.78	1.70 /0.96	2.90 /1.00	2.10 /1.00	3.39 /1.00	3.03 /1.00	0.2620	2.88 /1.00	5.96 /1.00
PIL163			2.92	2.42 /0.83	2.92 /1.01	2.11 /1.00	3.35 /0.99	2.88 /0.95	0.2866	2.55 /0.89	5.20 /0.87
PIL178			2.54	1.97 /0.78	3.03 /1.04	2.17 /1.03	3.47 /1.03	3.13 /1.03	0.3516	1.99 /0.69	3.90 /0.65
PIL177			2.85	1.90 /0.67	3.05 /1.05	2.18 /1.04	3.45 /1.02	2.96 /0.97	0.3250	2.24 /0.78	4.44 /0.75
PIL007			2.13	1.33 /0.62	3.06 /1.06	2.19 /1.04	3.42 /1.01	3.08 /1.02	0.3898	1.74 /0.60	3.33 /0.56

Table 3(c) Summary of measured and estimated bulk stress for undeformed sample and uniaxial compression experiments with constant displacement rate at -30 °C

Sample No.	T (°C)	Initial strain rate (s^{-1})	Measured peak stress (MPa)	Measured stress (MPa) at maximum strain, absolute /normalised	Estimated stress (MPa), absolute/normalised		Dislocation+GBS model (simplified Goldsby-Kohlstedt composite flow law)		Bulk reduced Schmid factor, S_{bulk}	Estimated stress (MPa), absolute/normalised	
										Azuma's flow law	
					Glen's flow law	**Durham's flow law**	Stress (MPa) modelled from grain size distribution, absolute /normalised	Stress (MPa) modelled from median grain size, absolute /normalised		With upper bound of ***B***	With lower bound of ***B***
PIL165	-30	$\sim 1 \times 10^{-5}$	8.24	8.15 /0.99	6.20 /1.00	5.01 /1.00	5.93 /1.00	5.81 /1.00	0.2443	6.84 /1.00	14.38 /1.00
PIL162			8.71	7.87 /0.90	6.22 /1.00	5.02 /1.00	5.92 /1.00	5.76 /0.99	0.2600	6.29 /0.92	13.06 /0.91
PIL164			8.93	7.31 /0.84	6.16 /0.99	4.99 /1.00	5.89 /0.99	5.64 /0.97	0.2742	5.79 /0.85	11.88 /0.83
PIL166			7.60	6.45 /0.85	6.41 /1.03	5.13 /1.02	6.01 /1.01	5.77 /0.99	0.2821	5.78 /0.84	11.80 /0.82
PIL268			7.82	5.00 /0.64	6.60 /1.06	5.25 /1.05	6.19 /1.05	5.70 /0.99	0.3040	5.36 /0.78	10.78 /0.75
PIL266	-30	$\sim 5 \times 10^{-5}$	11.29	11.26 /1.00	10.57 /1.00	7.47 /1.00	8.86 /1.00	8.81 /1.00	0.2586	10.78 /1.00	22.38 /1.00
PIL243			10.63	7.35 /0.69	11.36 /1.07	7.89 /1.06	9.32 /1.05	9.05 /1.03	0.3010	9.37 /0.87	18.88 /0.84

Table 4 Summary of strain rate, stress, and grain size of data from this study and the literature

Study	Sample No.	T (°C)	[1]True axial strain	[2]Initial grain size (μm)	[3]Measured strain rate (s^{-1})	[4]Converted strain rate (s^{-1})	Strain rate estimated from deformation mechanism maps	[5]Measured grain size, d-μm; A-mm^2	Converted grain size (μm)	[6]Measured stress at the end of experiments (MPa)	[7]Converted stress (MPa)
This study	OIL009	-4	0.01	297	$\dot{\varepsilon}$=1.11E-06	1.11E-06	1.10E-06	d=501	501	σ=1.02	1.02
	OIL008		0.04		Not recorded		1.20E-06	d=453	453	σ=0.99	0.99
	OIL007		0.08		$\dot{\varepsilon}$=1.78E-06	1.78E-06	1.30E-06	d=411	411	σ=0.95	0.95
	OIL006		0.13		$\dot{\varepsilon}$=1.22E-06	1.22E-06	1.60E-06	d=337	337	σ=0.9	0.90
	PIL176	-10	0.03		$\dot{\varepsilon}$=1.04E-05	1.04E-05	2.21E-06	d=126	126	σ=1.7	1.70
	PIL163		0.05		$\dot{\varepsilon}$=1.06E-05	1.06E-05	6.73E-06	d=98	98	σ=2.42	2.42
	PIL178		0.08		$\dot{\varepsilon}$=1.19E-05	1.19E-05	3.37E-06	d=118	118	σ=1.97	1.97
	PIL177		0.12		$\dot{\varepsilon}$=1.21E-05	1.21E-05	4.00E-06	d=92	92	σ=1.9	1.90
	PIL007		0.19		$\dot{\varepsilon}$=1.22E-05	1.22E-05	1.99E-06	d=87	87	σ=1.33	1.33
	PIL165	-30	0.03		$\dot{\varepsilon}$=1.09E-05	1.09E-05	4.04E-05	d=103	103	σ=8.15	8.15
	PIL162		0.05		$\dot{\varepsilon}$=1.10E-05	1.10E-05	3.61E-05	d=78	78	σ=7.87	7.87
	PIL164		0.07		$\dot{\varepsilon}$=1.07E-05	1.07E-05	2.80E-05	d=64	64	σ=7.31	7.31
	PIL166		0.12		$\dot{\varepsilon}$=1.20E-05	1.20E-05	1.81E-05	d=55	55	σ=6.45	6.45
	PIL268		0.21		$\dot{\varepsilon}$=1.31E-05	1.31E-05	8.65E-06	d=38	38	σ=5	5.00
	PIL266		0.03		$\dot{\varepsilon}$=5.40E-05	5.40E-05	1.43E-04	d=115	115	σ=11.26	11.26
	PIL243		0.24		$\dot{\varepsilon}$=6.70E-05	6.70E-05	3.16E-05	d=39	39	σ=7.35	7.35
Jacka & Maccagnan (1984)	A1	-3	0.01	2260	$\dot{\gamma}_{oc}$=2.00E-08	2.84E-08	6.33E-08	d=2200	2200	τ_{oc}=0.2	0.42
	A2		0.03		$\dot{\gamma}_{oc}$=3.60E-08	5.17E-08	5.15E-08	d=2800	2800	τ_{oc}=0.2	0.42
	A3		0.04		$\dot{\gamma}_{oc}$=4.00E-08	5.77E-08	4.77E-08	d=3100	3100	τ_{oc}=0.2	0.42
	A4		0.10		$\dot{\gamma}_{oc}$=6.10E-08	9.04E-08	4.07E-08	d=3900	3900	τ_{oc}=0.2	0.42
	A5		0.11		$\dot{\gamma}_{oc}$=6.30E-08	9.37E-08	3.69E-08	d=4600	4600	τ_{oc}=0.2	0.42
	A6		0.22		$\dot{\gamma}_{oc}$=6.10E-08	9.53E-08	3.69E-08	d=4600	4600	τ_{oc}=0.2	0.42
	A7		0.51		$\dot{\gamma}_{oc}$=6.00E-08	1.02E-07	3.69E-08	d=4600	4600	τ_{oc}=0.2	0.42
Jacka & Li (1994)	N/A	-3	>0.15	1240	$\dot{\gamma}_{oc}$=1.10E-07	N/A	8.65E-08	A=2	1596	τ_{oc}=0.2	0.42
				1240	$\dot{\gamma}_{oc}$=2.20E-07		2.56E-07	A=1.8	1514	τ_{oc}=0.3	0.64
				1240	$\dot{\gamma}_{oc}$=6.40E-07		6.30E-07	A=1.5	1382	τ_{oc}=0.4	0.85
				1240	$\dot{\gamma}_{oc}$=1.10E-06		1.65E-06	A=0.6	874	τ_{oc}=0.5	1.06
				1240	$\dot{\gamma}_{oc}$=2.60E-06		2.88E-06	A=0.6	874	τ_{oc}=0.6	1.27
				1240	$\dot{\gamma}_{oc}$=8.80E-06		9.61E-06	A=0.2	505	τ_{oc}=0.8	1.70
				2300	$\dot{\gamma}_{oc}$=6.00E-08		3.46E-08	A=21.2	5195	τ_{oc}=0.2	0.42
				2500	$\dot{\gamma}_{oc}$=1.32E-07		2.84E-07	A=1.4	1335	τ_{oc}=0.3	0.64
				2900	$\dot{\gamma}_{oc}$=1.12E-07		3.29E-07	A=1	1128	τ_{oc}=0.3	0.64
				2900	$\dot{\gamma}_{oc}$=9.50E-08		3.66E-07	A=0.8	1009	τ_{oc}=0.3	0.64
				1700	$\dot{\gamma}_{oc}$=3.25E-08		1.05E-07	A=1.4	1335	τ_{oc}=0.2	0.42
				798	$\dot{\gamma}_{oc}$=2.43E-07		2.46E-07	A=2	1596	τ_{oc}=0.3	0.64
				798	$\dot{\gamma}_{oc}$=2.54E-07		2.84E-07	A=1.4	1335	τ_{oc}=0.3	0.64
				798	$\dot{\gamma}_{oc}$=3.63E-07		6.49E-08	A=3.6	2141	τ_{oc}=0.2	0.42

		-5		1240	$\dot{\gamma}_{oc}$=6.00E-08		3.60E-08	A=2.7	1854	τ_{oc}=0.2	0.42
				1240	$\dot{\gamma}_{oc}$=3.30E-07		3.61E-07	A=1.1	1184	τ_{oc}=0.4	0.85
				1240	$\dot{\gamma}_{oc}$=1.40E-06		1.50E-06	A=0.7	944	τ_{oc}=0.6	1.27
				1240	$\dot{\gamma}_{oc}$=5.60E-06		4.20E-06	A=0.6	874	τ_{oc}=0.8	1.70
				1240	$\dot{\gamma}_{oc}$=1.30E-05		1.09E-05	A=0.2	505	τ_{oc}=1	2.12
				1600	$\dot{\gamma}_{oc}$=6.67E-08		7.94E-08	A=1.7	1471	τ_{oc}=0.25	0.53
				1600	$\dot{\gamma}_{oc}$=6.42E-08		7.04E-08	A=2.3	1711	τ_{oc}=0.25	0.53
				1600	$\dot{\gamma}_{oc}$=6.79E-08		7.43E-08	A=2	1560	τ_{oc}=0.25	0.53
		-10		1240	$\dot{\gamma}_{oc}$=7.00E-09		6.52E-09	A=1.7	1471	τ_{oc}=0.2	0.42
				1240	$\dot{\gamma}_{oc}$=4.80E-08		1.88E-08	A=2.1	1635	τ_{oc}=0.3	0.64
				1240	$\dot{\gamma}_{oc}$=9.80E-08		5.54E-08	A=1.1	1184	τ_{oc}=0.4	0.85
				1240	$\dot{\gamma}_{oc}$=2.00E-07		1.18E-07	A=1	1128	τ_{oc}=0.5	1.06
				1240	$\dot{\gamma}_{oc}$=3.80E-07		2.26E-07	A=0.9	1071	τ_{oc}=0.6	1.27
				2718	$\dot{\gamma}_{oc}$=2.90E-08		2.04E-08	A=1.6	1427	τ_{oc}=0.3	0.64
				2718	$\dot{\gamma}_{oc}$=7.20E-08		5.85E-08	A=0.9	1071	τ_{oc}=0.4	0.85
				2718	$\dot{\gamma}_{oc}$=3.50E-08		2.35E-07	A=0.7	944	τ_{oc}=0.6	1.27
				2718	$\dot{\gamma}_{oc}$=1.10E-08		6.83E-07	A=0.5	798	τ_{oc}=0.8	1.70
				2718	$\dot{\gamma}_{oc}$=3.60E-08		1.63E-06	A=0.3	618	τ_{oc}=1	2.12
Vaughan et al. (2017)	def014	-5	0.01	343	$\dot{e}$=1.00E-06	1.01E-06	2.50E-06	d=355	355	σ=1.12	1.12
	def013		0.03			1.03E-06	1.52E-06	d=425	425	σ=1.13	1.13
	def012		0.05			1.05E-06	9.11E-07	d=364	364	σ=1.22	1.22
	def011		0.08			1.08E-06	4.43E-07	d=349	349	σ=1.17	1.17
	def010		0.11			1.11E-06	2.10E-07	d=377	377	σ=1.2	1.2
Fan et al. (2020)	PIL254	-20	0.03	297	$\dot{\varepsilon}$=1.06E-05	1.06E-05	1.31E-05	d=62	62	σ=4.25	4.25
	PIL182		0.04		$\dot{\varepsilon}$=8.94E-06	8.94E-06	1.32E-05	d=122	122	σ=4.44	4.44
	PIL184		0.08		$\dot{\varepsilon}$=1.17E-05	1.17E-05	4.53E-06	d=89	89	σ=3.24	3.24
	PIL185		0.12		$\dot{\varepsilon}$=1.19E-05	1.19E-05	8.61E-06	d=53	53	σ=3.68	3.68
	PIL255		0.20		$\dot{\varepsilon}$=1.28E-05	1.28E-05	4.25E-06	d=53	53	σ=2.93	2.93

[1] Strain at the end of uniaxial compression experiment is converted to true axial strain following methods described by Fan et al. (2020).

[2] Initial grain size is median grain size for data from this study, Vaughan et al. (2017) and Fan et al. (2020). Initial grain size is taken directly from Jacka & Maccagnan (1984), and it is calculated using mean linear intercept method (Appendix E). Initial grain size is converted from averaged grain area by Eq. (E.2) for data from Jacka & Li (1994).

[3] $\dot{\varepsilon}$ is true axial strain rate. $\dot{\gamma}_{oc}$ is octahedral shear strain rate. $\dot{e}$ is engineering strain rate.

[4] $\dot{\gamma}_{oc}$ and $\dot{e}$ are converted to $\dot{\varepsilon}$ using methods described by Fan et al. (2020).

[5] Measured grain size is median grain size for data from this study, Vaughan et al. (2017) and Fan et al. (2020). Measured grain size is taken directly from Jacka & Maccagnan (1984), and it is calculated using mean linear intercept method (Appendix E). Measured grain size is converted from averaged grain area by Eq. (E.2) for data from Jacka & Li (1994).

[6] σ is differential axial stress. $\tau_{oc}$is octahedral shear stress.

[7] τ_{oc} is converted to σ using methods described by Fan et al. (2020).

Journal of Geophysical Research: Solid Earth

Supporting Information for

Crystallographic preferred orientation (CPO) development governs the strain weakening in minerals with strong viscous anisotropy at high homologous temperatures (≥ 0.9): insights from up-strain ice deformation experiments

Sheng Fan[1], Andrew J. Cross[2,3], David J. Prior[1], David L. Goldsby[2], Travis F. Hager[2], Marianne Negrini[1], Chao Qi[4]

[1] Department of Geology, University of Otago, Dunedin, New Zealand

[2] Department of Geology and Geophysics, Woods Hole Oceanographic Institution, Woods Hole, MA, USA

[3] Department of Earth and Environmental Science, University of Pennsylvania, Philadelphia, PA, USA

[4] Institute of Geology and Geophysics, Chinese Academy of Sciences, Beijing, China

Contents of this file

Introduction

The supporting information includes:

(1) A comparison between modelled mechanical data using the Azuma's flow law with the input of reduced Schmid factors calculated from different methods (Sect. S1).

(2) A summary on the percentage of stress-drop from peak to the flow stresses from published ice uniaxial compression experiments with constant displacement rates (Sect. S2).

(3) Full detailed data sets that summarize the relative contribution of CPO development and grain size change to the strain weakening from this study and published literature. These data sets are used for the plotting of Fig. 8 (Sect. S3).

Section S1 Comparing modelled mechanical data using the Azuma's flow law with the input of reduced Schmid factors calculated from different methods

Table S1(a) Constant load experiments

Sample No.	Bulk reduced Schmid factor, S_{bulk} (Eq. (12))	Estimated strain rate (s^{-1}) using S_{bulk}, absolute/normalised		Number weighted mean Schmid factor, $\bar{S}$ ($=\frac{1}{N}\sum S$)	Estimated strain rate (s^{-1}) using $\bar{S}$, absolute/normalised	
		With upper bound of $^{\#}\boldsymbol{B}$	With lower bound of $\boldsymbol{B}$		With upper bound of $\boldsymbol{B}$	With lower bound of $\boldsymbol{B}$
OIL009	0.2514	6.92×10^{-7} /1.00	7.59×10^{-8} /1.00	0.3368	2.36×10^{-6} /1.00	3.10×10^{-7} /1.00
OIL008	0.3239	2.01×10^{-6} /2.90	2.56×10^{-7} /3.37	0.406	5.18×10^{-6} /2.19	7.58×10^{-7} /2.45
OIL007	0.3295	2.16×10^{-6} /3.12	2.78×10^{-7} /3.66	0.4119	5.51×10^{-6} /2.33	8.12×10^{-7} /2.63
OIL006	0.3766	3.78×10^{-6} /5.46	5.28×10^{-7} /6.96	0.4377	7.11×10^{-6} /3.01	1.10×10^{-6} /3.52

Table S1(b) Constant displacement rate experiments

Sample No.	Bulk reduced Schmid factor, S_{bulk}	Estimated stress (MPa), absolute/normalised		Number weighted mean Schmid factor, $\bar{S}$	Estimated stress (MPa), absolute/normalised	
		With upper bound of $\boldsymbol{B}$	With lower bound of $\boldsymbol{B}$		With upper bound of $\boldsymbol{B}$	With lower bound of $\boldsymbol{B}$
PIL176	0.2620	2.88 /1.00	5.96 /1.00	0.3320	2.07 /1.00	4.08 /1.00
PIL163	0.2866	2.55 /0.89	5.20 /0.87	0.3779	1.73 /0.84	3.34 /0.82
PIL178	0.3516	1.99 /0.69	3.90 /0.65	0.4107	1.60 /0.78	3.04 /0.74
PIL177	0.3250	2.24 /0.78	4.44 /0.75	0.4034	1.65 /0.80	3.14 /0.77
PIL007	0.3898	1.74 /0.60	3.33 /0.56	0.4354	1.49 /0.72	2.79 /0.68
PIL165	0.2443	6.84 /1.00	14.38 /1.00	0.3227	4.64 /1.00	9.21 /1.00
PIL162	0.2600	6.29 /0.92	13.06 /0.91	0.3421	4.29 /0.92	8.42 /0.91
PIL164	0.2742	5.79 /0.85	11.88 /0.83	0.3619	3.92 /0.85	7.62 /0.83
PIL166	0.2821	5.78 /0.84	11.80 /0.82	0.3651	4.03 /0.87	7.81 /0.85
PIL268	0.3040	5.36 /0.78	10.78 /0.75	0.3674	4.11 /0.89	7.96 /0.86
PIL266	0.2586	10.78 /1.00	22.38 /1.00	0.3461	7.17 /1.00	14.14 /1.00
PIL243	0.3010	9.37 /0.87	18.88 /0.84	0.3775	6.82 /0.95	13.13 /0.93

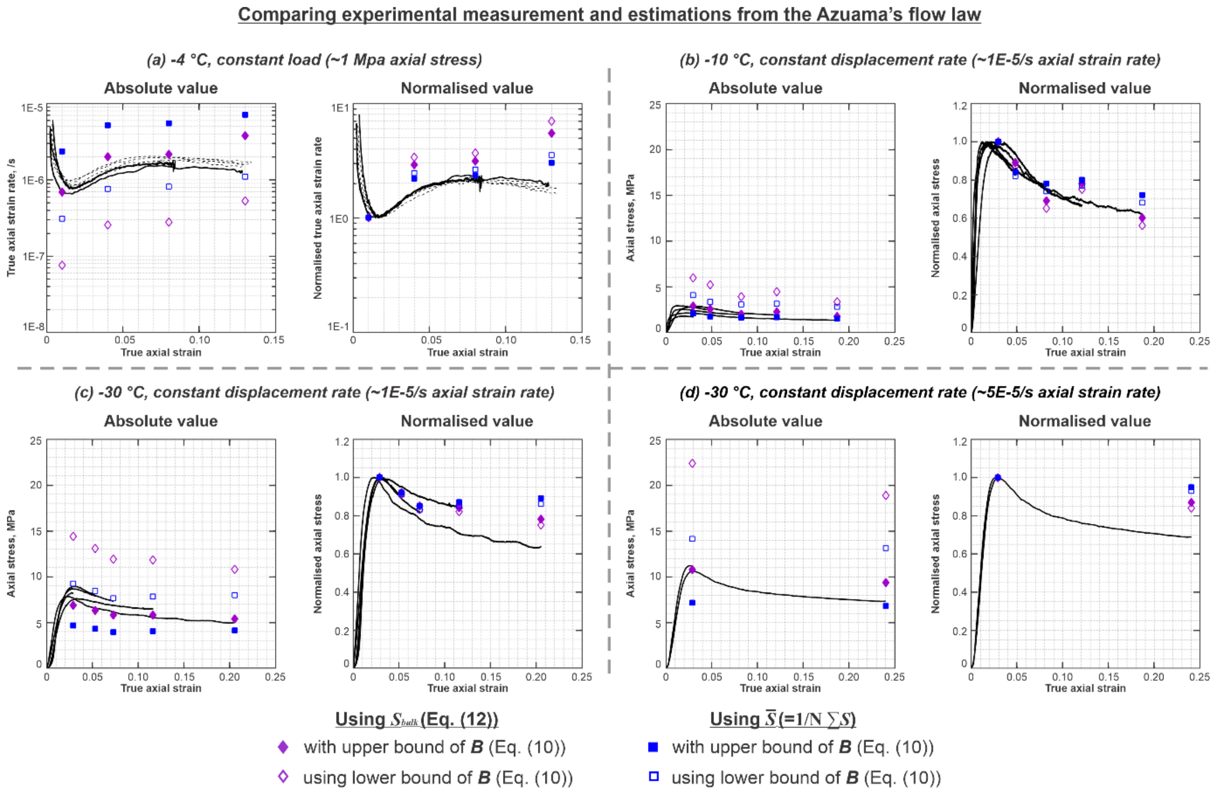

Figure S1. Comparing the ice mechanical behaviours estimated from the Azuma's flow law using the bulk reduced Schmid factor, S_{bulk} (Eq. (12)) and the number weighted mean reduced Schmid factor ($\bar{S} = \frac{1}{N}\sum S$). Full data are listed in Tables S1(a), S1(b).

Section S2 The stress drop from peak to flow stress in constant displacement rate experiments

Table S2. Summary of the stress drop from peak to flow stress in published constant displacement rate experiments

Study	Sample No.	Percentage of stress drop from peak to flow stress (%)	Peak stress (MPa)	Flow stress (MPa)	T (K)	Strain	Strain rate (s^{-1})	Average initial grain size (μm)
Durham et al. (1983)	37	19.54	65.50	52.70	195	0.158	3.5×10^{-4}	1000-2000
	38	22.76	63.70	49.20	195	0.140	3.5×10^{-4}	1000-2000
	39	16.04	58.60	49.20	195	0.196	3.5×10^{-4}	1000-2000
	40	35.04	48.80	31.70	195	0.170	3.5×10^{-4}	1000-2000
	41	59.38	25.60	10.40	195	0.241	3.5×10^{-4}	1000-2000
	43	37.64	51.80	32.30	195	0.395	3.5×10^{-4}	1000-2000
	70-1	51.39	14.40	7.00	258	0.135	3.5×10^{-4}	1000-2000
Durham et al. (1992)	188	45.38	36.80	20.10	223	0.216	4.4×10^{-4}	600-1000
	189	30.14	28.20	19.70	223	0.220	4.4×10^{-4}	600-1000
	192	38.06	36.00	22.30	223	0.237	4.5×10^{-4}	1000-2000
	193	38.99	33.60	20.50	223	0.275	4.7×10^{-4}	180-250
	195	43.28	87.80	49.80	179	0.169	4.1×10^{-5}	180-250
	197	21.09	81.10	64.00	179	0.151	4.0×10^{-5}	1000-2000

	205	33.39	54.80	36.50	180	0.187	4.0×10^{-6}	1000-2000
	206	45.80	60.70	32.90	180	0.193	4.1×10^{-6}	600-1000
	210	50.60	58.30	28.80	179	0.195	4.1×10^{-6}	180-250
	211	30.27	105.70	73.70	179	0.141	3.8×10^{-4}	600-1000
	212	34.07	112.70	74.30	179	0.140	3.8×10^{-4}	180-250
	216	22.24	119.60	93.00	159	0.117	3.7×10^{-5}	600-1000
Piazolo et al. (2013)	MD6	18.70	1.23	1.00	266	0.100	6.0×10^{-7}	500
	MD3	33.81	2.10	1.39	266	0.200	2.5×10^{-6}	500
	MD4	40.00	3.10	1.86	266	0.200	1.0×10^{-5}	500
Vaughan et al. (2017)	def10	61.86	1.18	0.45	268	0.100	1.0×10^{-6}	350
Qi et al. (2017)	PIL7	29.41	2.55	1.80	263	0.180	1.1×10^{-5}	230
	PIL32	29.73	1.85	1.30	263	0.210	2.1×10^{-6}	230
	PIL33	46.72	8.09	4.31	263	0.220	2.2×10^{-4}	230
	PIL35	33.94	3.30	2.18	263	0.130	1.2×10^{-5}	230
	PIL36	44.28	5.42	3.02	263	0.190	5.0×10^{-5}	230
	PIL18	47.53	2.23	1.17	263	0.180	1.2×10^{-6}	630
	PIL19	52.35	6.17	2.94	263	0.230	4.0×10^{-5}	630
	PIL20	54.14	7.61	3.49	263	0.230	8.5×10^{-5}	630
	PIL21	51.62	4.01	1.94	263	0.230	1.1×10^{-5}	630

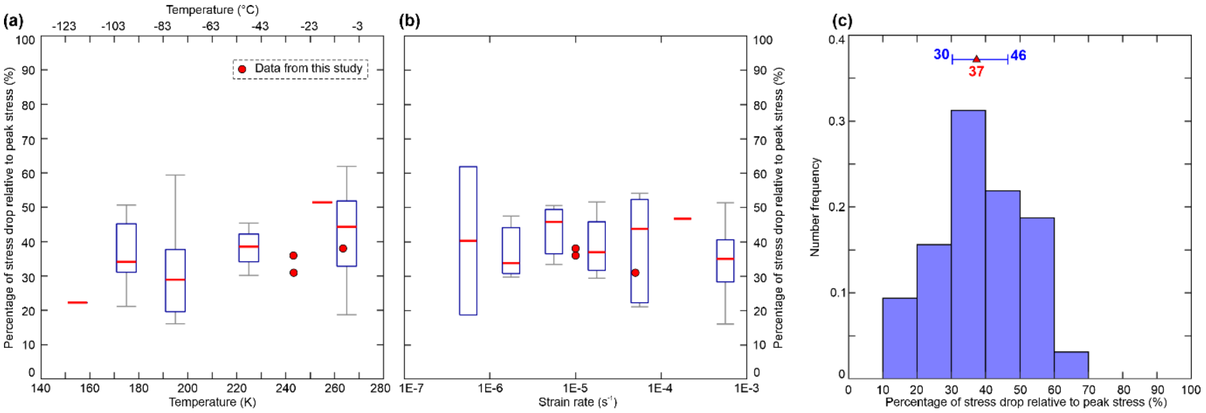

Figure S2. (a) Box plots representing the distribution of the percentage of stress drop from peak to flow stress at each temperature interval, from published data (Table S2). The blue box covers the interquartile range and represents 50% of the total data, the red line within the box is the median point and the whiskers are the extremes (3/2s of the interquartile range). Points represent data from this study. **(b)** Box plots representing the distribution of the percentage of stress drop from peak to flow stress at each strain rate interval, from published data (Table S2). The x-axis is in log-scale. Points represent data from this study. **(c)** Bar plot representing the distribution of the percentage of stress drop from peak to flow stress, from published data (Table S2). Error bar above the bar plot representing the interquartile range (50% of the total data), constrained by blue whiskers, and the median value, shown as red triangle.

Section S3 Full details of for the relative contribution of CPO development and grain size change to the strain weakening (Sect. 4.2.3), corresponding to Fig. 8

Table S3(a) Compare the relative contribution of CPO development and grain size change to the strain weakening for constant load/stress experiments

Study	Sample No.	True axial strain	[1]Average grain size (μm)	Bulk reduced Schmid factor, S_{bulk}	Measured normalised strain rate ($\bar{\dot{\varepsilon}}_{measure}$)	Modelled strain rate (/s)		Modelled normalised strain rate		$\frac{\bar{\dot{\varepsilon}}_{measure}}{\bar{\dot{\varepsilon}}_{model}(Disl.+GBS)}$	$\frac{\bar{\dot{\varepsilon}}_{measure}}{\bar{\dot{\varepsilon}}_{model}(Azuma)}$
						Dislocation+GBS model ($\dot{\varepsilon}_{model}$ $(Disl.+GBS)$)	[2]Azuma's flow law ($\dot{\varepsilon}_{model}$ $(Azuma)$)	Dislocation+GBS model ($\bar{\dot{\varepsilon}}_{model}$ $(Disl.+GBS)$)	Azuma's flow law ($\bar{\dot{\varepsilon}}_{model}$ $(Azuma)$)		
Jacka & Maccagnan (1984)	A1	0.01	2200	0.2759	1.0	6.33E-08	8.43E-8	1.0	1.0	1.0	1.0
	A2	0.03	2800	0.3055	1.82	5.15E-08	1.29E-7	0.84	1.54	2.17	1.19
	A3	0.04	3100	0.3351	2.03	4.77E-08	1.91E-7	0.79	2.26	2.59	0.90
	A4	0.10	3900	0.3736	3.18	4.07E-08	3.01E-7	0.69	3.57	4.62	0.89
	A5	0.11	4600	0.3561	3.30	3.69E-08	2.46E-7	0.64	2.92	5.18	1.13
	A6	0.22	4600	0.4032	3.36	3.69E-08	4.15E-7	0.64	4.92	5.27	0.68
	A7	0.51	4600	0.3965	3.59	3.69E-08	3.87E-7	0.64	4.59	5.64	0.78
This study	OIL009	0.01	501	0.2514	1.0	1.10E-06	6.92E-7	1.0	1.0	1.0	1.0
	OIL008	0.04	453	0.3239	1.68	1.20E-06	2.01E-6	1.09	2.90	1.54	0.58
	OIL007	0.08	411	0.3295	2.35	1.30E-06	2.16E-6	1.19	3.12	1.97	0.75
	OIL006	0.13	337	0.3766	1.87	1.60E-06	3.78E-6	1.45	5.46	1.29	0.34

[1] Average grain size is median grain size for data from this study. Average grain size from Jacka & Maccagnan (1984) is calculated using mean linear intercept method (Appendix E).

2 The strain rate modelled from the Azuma's flow law is calculated using the upper bond of pre-exponential term, B (Sect. 2.3.3; Eqs. (8), (10)).

Table S3(b) Compare the relative contribution of CPO development and grain size change to the strain weakening for constant displacement rate experiments

Study	Sample No.	True axial strain	[1]Average grain size (μm)	Bulk reduced Schmid factor, S_{bulk}	Measured normalised stress drop ($\Delta\bar{\sigma}_{measure}$)	Modelled stress (MPa)		Modelled normalised stress drop		$\frac{\Delta\bar{\sigma}_{measure}}{\Delta\bar{\sigma}_{model}(Disl.+GBS)}$	$\frac{\Delta\bar{\sigma}_{measure}}{\Delta\bar{\sigma}_{model}(Azuma)}$
						Dislocation+GBS model (σ_{model} $(Disl.+GBS)$)	[2]Azuma's flow law (σ_{model} $(Azuma)$)	Dislocation+GBS model ($\Delta\bar{\sigma}_{model}$ $(Disl.+GBS)$)	Azuma's flow law ($\Delta\bar{\sigma}_{model}$ $(Azuma)$)		
Vaughan et al. (2017)	def014	0.01	355	0.2345	0.0	0.97	1.30	N/A	N/A	N/A	N/A
	def013	0.03	425	0.2753	0.04	0.99	1.04	-0.020	0.20	-1.97	0.22
	def012	0.05	364	0.3396	0.34	0.98	0.77	-0.006	0.41	-60.39	0.85
	def011	0.08	349	0.3666	0.50	0.92	0.69	0.050	0.47	10.24	1.08
	def010	0.11	377	0.3908	0.67	0.97	0.64	-0.002	0.51	-335.68	1.30
#Qi et al. (2017)	PIL032	0.21	N/A	0.4053	0.30	N/A	0.95	N/A	0.49	N/A	0.61
	PIL033	0.22		0.2986	0.47		6.84		0.17		2.72
	PIL035	0.13		0.3521	0.34		2.08		0.35		0.98
	PIL036	0.19		0.3424	0.44		3.34		0.34		1.31
This study	PIL176	0.03	291	0.2620	0.0	3.03	2.88	0.0	0.0	0.0	0.0
	PIL163	0.05	126	0.2866	0.11	2.88	2.55	0.050	0.11	3.32	1.54
	PIL178	0.08	98	0.3516	0.31	3.13	1.99	-0.030	0.31	-7.12	0.74
	PIL177	0.12	118	0.3250	0.22	2.96	2.24	0.030	0.22	12.89	1.49
	PIL007	0.19	92	0.3898	0.40	3.08	1.74	-0.020	0.40	-22.75	0.96
	PIL165	0.03	87	0.2443	0.0	5.81	6.84	0.0	0.0	0.0	0.0
	PIL162	0.05	103	0.2600	0.08	5.76	6.29	0.009	0.08	10.44	1.20
	PIL164	0.07	78	0.2742	0.15	5.64	5.79	0.029	0.15	6.22	1.17
	PIL166	0.12	64	0.2821	0.16	5.77	5.78	0.007	0.16	19.87	0.97
	PIL268	0.21	55	0.3040	0.22	5.70	5.36	0.020	0.22	18.62	1.68
	PIL266	0.03	38	0.2586	0.0	8.81	10.78	0.0	0.0	0.0	0.0
	PIL243	0.24	115	0.3010	0.23	9.05	9.37	-0.027	0.16	-11.39	2.00

[1] Average grain size is median grain size for data from this study, Vaughan et al. (2017), and Qi et al. (2017).

[2] The stress modelled from the Azuma's flow law is calculated using the upper bond of pre-exponential term, B (Sect. 2.3.3; Eqs. (8), (10)).

Qi et al. (2017) only provides microstructural data at ~20% strain. Each sample's grain size at peak stress is unpredictable (Sect. 4.2.3), therefore, we cannot estimate the stress drop using the Dislocation+GBS model. The estimated stress drop using Azuma's flow law assumes the CPO is random at peak stress (Sect. 4.2.3).

References

Durham, W B, Heard, H. C., & Kirby, S. H. (1983). Experimental deformation of polycrystalline H 2 O ice at high pressure and low temperature: Preliminary results. *Journal of Geophysical Research*, *88*(S01), B377. https://doi.org/10.1029/JB088iS01p0B377

Durham, William B., Kirby, S. H., & Stern, L. A. (1992). Effects of dispersed particulates on the rheology of water ice at planetary conditions. *Journal of Geophysical Research*, *97*(E12), 20883. https://doi.org/10.1029/92je02326

Jacka, T. H., & Maccagnan, M. (1984). Ice crystallographic and strain rate changes with strain in compression and extension. *Cold Regions Science and Technology*, *8*(3), 269–286. https://doi.org/10.1016/0165-232X(84)90058-2

Piazolo, S., Wilson, C. J. L., Luzin, V., Brouzet, C., & Peternell, M. (2013). Dynamics of ice mass deformation: Linking processes to rheology, texture, and microstructure. *Geochemistry, Geophysics, Geosystems*, *14*(10), 4185–4194. https://doi.org/10.1002/ggge.20246

Qi, C., Goldsby, D. L., & Prior, D. J. (2017). The down-stress transition from cluster to cone fabrics in experimentally deformed ice. *Earth and Planetary Science Letters*, *471*, 136–147. https://doi.org/10.1016/j.epsl.2017.05.008

Vaughan, M. J., Prior, D. J., Jefferd, M., Brantut, N., Mitchell, T. M., & Seidemann, M. (2017). Insights into anisotropy development and weakening of ice from in situ P wave velocity monitoring during laboratory creep. *Journal of Geophysical Research: Solid Earth*, *122*(9), 7076–7089. https://doi.org/10.1002/2017JB013964